University of California
Santa Barbara

Continuum Simulations of Multi-Cellular Tumor Spheroids using Two-phase Flow Models

A Thesis submitted in partial satisfaction
of the requirements for the degree

Master of Science
in
Mechanical Engineering

by

Dennis Manjaly Joshy

Committee in charge:

Professor Otger Campàs, Chair
Professor Carl Meinhart
Professor Enoch Yeung

September 2019

The Master's Thesis of Dennis Manjaly Joshy is approved.

Professor Carl Meinhart

Professor Enoch Yeung

Professor Otger Campàs, Committee Chair

September 2019

Continuum Simulations of Multi-Cellular Tumor Spheroids using Two-phase Flow Models

by

Dennis Manjaly Joshy

Dedicated to my Mother, Father and David

Acknowledgements

I would like to first, thank my advisor Prof. Otger Campàs for allowing me to work in the Campàs lab. I would like to express my gratitude to him for mentoring me to, not only become a good physicist but also in experimental techniques and necessary presentation skills. I would like to thank Prof. Carl Meinhart for teaching me to use COMSOL, both via courses at UCSB and also outside. I would like to thank Prof. Enoch Yeung for providing me fresh perspectives in cancer behavior and potential avenues of future research by integrating synthetic biology with it.

I thank Carlos Gomez of the Campàs lab for teaching me several experimental skills including cell culture techniques, transfection, microscopy and protocols for generating oil droplet-based sensors. I thank him for teaching to troubleshoot experiments and to use image processing software to notice interesting patterns. I thank Dr. Payam Rowghanian and Dr. Samhita Banavar for helping with the simulations and providing me a platform to discuss related problems and exchange ideas. They offered me an opportunity to work in a diverse class of Finite Element Method problems that are still largely unexplored, but important for the field of mechanobiology. I thank all the members of the Campàs lab for teaching important technical skills, crucial lab etiquette and communication skills.

I thank the Application Engineers at COMSOL, Mina Sierou, Andy Cai and Ali Nojoumi. I greatly appreciate their inputs and their commitment to respond to all queries within one day. Finally, I would like to thank again all my colleagues in both the Campàs Lab and Yeung Lab and my friends Sreerag Mandakathil Sreenath, Allen Chacko and Aravind Uthaman and Balanarayan Suresh for their constant support and motivation to finish this work.

Abstract

Continuum Simulations of Multi-Cellular Tumor Spheroids using Two-phase Flow Models

by

Dennis Manjaly Joshy

Cancer growth and invasion is a problem that has been studied for several decades, particularly due to high mortality rates among patients. Despite this, large gaps in our understanding of cancer remain. The traditional approach for studying cancer has been largely from the biological perspective. But, recently, the biophysical properties of cancer have proven to complement these traditional studies and enhance our understanding of cancer. Are there mechanical gradients developed inside tumor aggregates? Do these gradients represent a solid-to-fluid phase transition inside the spheroid? If so, does it affect its behavior? How does the growth of the tumor aggregate affect its surface features? If so, are these features that could initiate tumor invasion? What is the involvement of the forces that the tumor exerts on its surroundings?

This study attempts to answer these questions by developing a simplified Stokes' flow model using the commercial Multiphysics package — COMSOL Multiphysics versions (5.3) and (5.4). It begins by highlighting the relevance of mechanics in cancer and notable attempts to model them mathematically. The internal mechanics of the tumor and the evolution of the spheroid contour as it grows has been discussed. We studied curvature dependent active stresses normal to the spheroid surface. Growth induced surface instabilities have also been explored. Experimental techniques that could be used to confirm these hypotheses have been described and finally, the potential future work in this domain has been elucidated.

Contents

Abstract **vi**

1 Introduction **1**
1.1 Cancer as a Dynamical System 1
1.2 The Mechanical Perspective of Cancer 4
1.3 Multi-Cellular Tumor Spheroids 8
1.4 Modeling Multi-Cellular Tumor spheroids 10

2 Two-phase Axisymetric Model of Tumor Growth **17**
2.1 Introduction 17
2.2 The Arbitrary Lagrangian-Eulerian Algorithm 18
2.3 Governing Differential Equations 19
2.4 Computational Domain 21
2.5 Relevant Dimensionless Parameters 22
2.6 Material Properties 23
2.7 Scaling the Governing Differential Equations 27
2.8 Implementing the Parametric Sweep 28
2.9 Results 29
2.10 Discussion 38
2.11 Conclusions 41

3 Two-phase model of Tumor spheroids applying Active Stresses **42**
3.1 Introduction 42
3.2 Computational Domains 43
3.3 Governing Differential Equations 43
3.4 Active Surface Stresses 45
3.5 Scaling of Equations 50
3.6 Computational Results 54
3.7 Discussion 60
3.8 Conclusion 63

4 Troubleshooting Experiments to validate theoretical models **64**
4.1 Introduction . . . 64
4.2 Experimental Setup . . . 65
4.3 Data Acquisition and Processing . . . 67
4.4 Cell Lines Used . . . 69
4.5 Culturing Flourescent Tagged MCTS . . . 69

5 Conclusions and Future Work **72**
5.1 Future Work . . . 73

A Cell Culture Methods **77**
A.1 Unfreezing Cells . . . 77
A.2 Passaging of Confluent Cell Lines . . . 78
A.3 Cryopreservation of Cell Lines . . . 80
A.4 Transfection of Cell Lines to Improve Imaging . . . 80
A.5 3D Cell Culture of Tumor Spheroids . . . 81
A.6 Culturing 3 Dimensional Multi-cellular Spheroids . . . 81

B Preparation of Sample **83**
B.1 Mixing the components for magnetic oil droplets . . . 83
B.2 Inserting the magnetic droplets into the spheroids . . . 84
B.3 Embedding the Spheroids in a Collagen Matrix . . . 85

Bibliography **88**

Chapter 1

Introduction

1.1 Cancer as a Dynamical System

Homeostasis is a Greek word which translates to "staying the same". More formally, from a biological standpoint, an organism can maintain its physiological conditions via biophysical and biochemical pathways. An example is that of how the human body controls the size of its organs. As organs are composed of tissues formed by cells arranged by morphogenesis, the body has to actively regulate cell division and apoptosis (programmed cell death) to maintain the correct organ size. In a living system, this is accomplished by natural control systems, manifested in the form of many signaling cascades in which proteins interact with each other to transmit information. The Hippo pathway is one of the signaling cascades which is conserved in many organisms that help maintain organ size. [1].

Cancer is a consequence of the disruption of cancer-suppressing control systems like the Hippo Pathway [2], [3]. One effect of this disruption is the cancer cells' ability to acquire the unlimited potential for cell division. Studies have shown that as the tumor's

size increases due to this, it recruits blood vessels to provide itself nutrition. This is also accompanied by significant remodeling of its surrounding micro-environment to facilitate invasion. Several biological and biophysical transitions eventually contribute to the tumor‘s acquisition of invasive characteristics. Today, it is known that cancer cells show ten specific biological hallmarks that allow them to thrive and actively migrate to a new organ site [4], [5]. The diversity of these hallmarks and the different scales of time and length at which they function make it difficult to predict the behavior of cancer. Finally, after having acquired these malignant traits, the cancer cells will make their way into lymph nodes and local vasculature. From this point, they can travel to distant organs and the process is termed as *metastasis*. Tumor metastasis is a complicated phenomenon in human health as it is the state at which the disease becomes nearly incurable. It has been extensively studied in many ways from a biochemical perspective; what is lacking is a novel perspective like a mechanical approach to understanding cancer.

Due to the high incidence rates of cancer, with nearly 18.1 million new cases in the year 2018 itself, tumor-suppressing pathways that are dysregulated and the proteins that constitute them have been extensively studied. The motives of these studies being to predict or to kill cancer cells or to induce cancer remission. However, large gaps in our understanding of cancer behavior remain. In a novel attempt to fill these gaps, scientists are currently examining a much more fundamental mode of cellular communication. This is mechanical perturbation and the changes in the tumor and tumor micro-environmental mechanics. Mechanical palpitation is a generally known technique used by medical practitioners as a rough diagnosis to detect tumors or tissues modified by tumors. At the cellular level, tumor cells exert and experience a myriad of mechanical stresses, both during their avascular stage and as they metastasize. While many of them are harmful to the cancer cells, they find ways to survive them [7]. These stresses are gradually be-

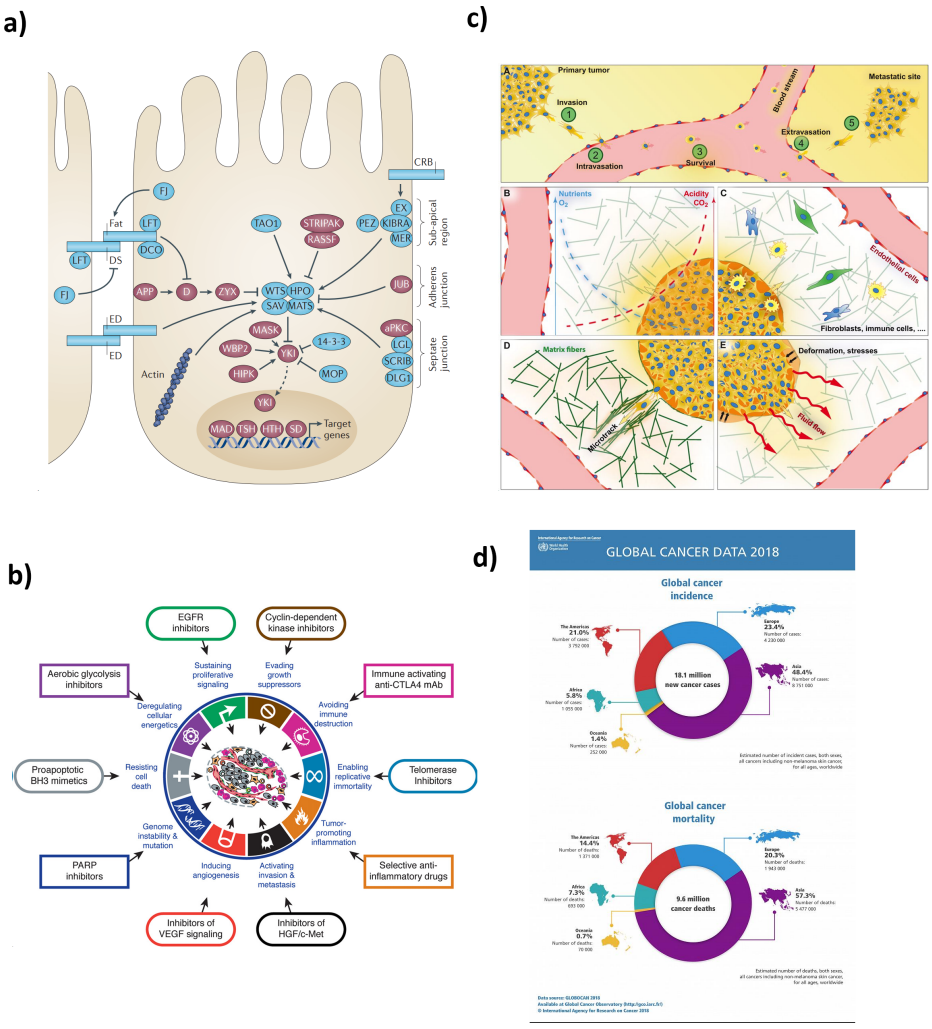

Figure 1.1: a) A network representation of how the Hippo Pathway takes input signals from junction proteins in addition to other extra-cellular inputs [2]. It is potentially a mechanosensitive pathway. b) The ten hallmarks of cancer as explained in [4], which helps cancer cells to thrive and invade. c) The five-step process by which a solid tumor invades and leaves its primary site. The mechanical properties and instabilities formed by the tumor during the initiation of invasion can provide novel insight into their working [6]. d) Cancer statistics from the World Health Organization demonstrated that cancer is among the deadliest diseases with almost a 50% mortality rate all over the world.

ginning to be understood via emerging interdisciplinary fields like mechanobiology. The growing interest in this area of research is further evidenced by the emergence of several institutions specializing in physical oncology.

Albeit, the concept of using mechanical palpitation appears rather unsophisticated, most advanced sensors used for mechanically characterizing living tissues work on the same principle. A force is applied to the biological system under study and its strain or strain-rate response is recorded. This information is fit to appropriate constitutive models.

Techniques for applying forces biological systems include Atomic Force Microscopy (AFM), Traction Force Microscopy (TFM), hydrogel-based sensors, droplet insert techniques, optical traps, etc. [8]. These techniques evolved over the past 30 years and have helped make cogent discoveries that highlight the role of mechanics and mechanical cues involved in morphogenesis, at both the cellular and the tissue level. However, they have hitherto not been employed in the study of cancer invasion. The droplet insert techniques developed in the Campàs lab is a technique that can make in-vivo measurements during organ/aggregate development [9]. These techniques are becoming more sophisticated as it is becoming more evident that mechanics play a crucial role in cancer progression as explained in the next section.

1.2 The Mechanical Perspective of Cancer

Mechanical cues can affect tumors from the nuclear level to the scale of the bulk tissues. Consider for instance the Hippo Pathway itself. The Yes-associated Protein (YAP) and the Transcriptional Co-activator with PDZ-binding motif (TAZ) are proteins functioning downstream of the Hippo Pathway. The translocation of these transcriptional co-activators into the nucleus influences cell proliferation, which might be linked to cancer. Dysregulation of the Hippo Pathway is observed in many types of cancers.

Studies using cancer cells have shown that increasing the growth substrate's stiffness has increased the transcriptional activity of YAP-TAZ. [10], [11]. In addition to affecting cell proliferation, mechanical cues can induce invasive characteristics too. Compressive stresses of the order of 0.2- 0.25 kPa have been shown to upregulate genes that facilitate proteolysis, which cancer cells perform to breakdown and remodel their surroundings. Some of these include *Cathespin B* and PTEN [12]. This provides evidence that the mechanics of the environment can induce changes in gene expression to the point that it can influence tumor-suppressing pathways.

Proteins serve multiple structural and catalytic functions. They can transmit both mechanical and chemical signals which can be critical for cancer cells. Mechanotransduction is the process by which the exterior mechanical cues are translated into chemical ones inside the cell. Such signals can profoundly impact the cell's functioning at the protein or genome level. For example, vinculin is a molecule that, in a force-dependent manner, recruits and releases relevant proteins that sequester at Focal Adhesions [13], [17]. The force transmitted via vinculin causes vinculin-binding-sites to become exposed. It has also been demonstrated that mechanotransduction via vinculin can interfere with the functioning of integrins. Integrins are proteins that with the help of Focal Adhesions help to maintain the attachment of a mammalian cell to its substrate. Disruption of integrins can be involved in Epithelial-to-Mesenchymal Transitions (EMT), which is a well-known trait exhibited by many cancerous cells [18], [19], [20]. Cancer cells are proven to undergo significant morphological changes as they begin invasion or metastasis. The overall mechanical properties of a tumor cell can influence its metastatic potential. For example, it has been demonstrated that HEY cells, which are more compliant than other cells have relatively higher invasion levels than others. [14]. In this study, magnetic tweezers were used to apply known forces on 2.8 μm diameter beads attached to cells and the resultant displacements were measured.

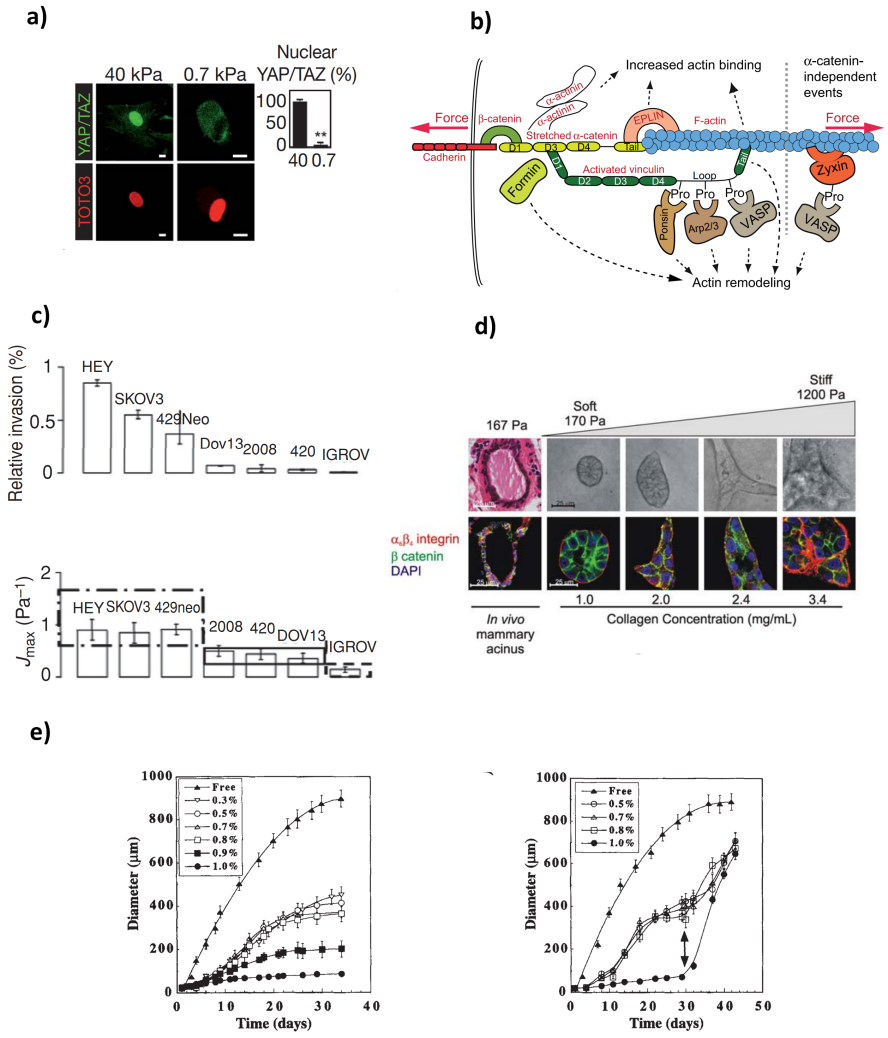

Figure 1.2: a) Fluorescence image showing that nuclear translocation of YAP-TAZ increases with substrate stiffness. Mechanical cues from the environment might be able to influence gene expressions [10], b) A schematic representation of the involvement of vinculin in recruiting proteins upon activation due to an applied force [13]. c) Bar graphs demonstrating that tumor cells demonstrating high invasion propensities (top graph) exhibit high compliance (lower graph) [14]. d) Breast tumorigenesis increases with substrate stiffness - implying the role of mechanics on the level of cell colonies [15]. e) Higher compressive stresses and gel concentration can lead to smaller spheroids, indicating the influence of mechanics in 3 dimensions [16]

A description of the mechanics of tumor invasion is incomplete without analyzing the mechanical transitions experienced by the tumor micro-environment. Several theoretical and experimental studies have concluded that the invasive potential of a tumor aggregate increases with the stiffness of the tumor-microenvironment [21]. Breast tumorigenesis has been shown to increase due to the stiffening of the collagen substrate using Ribose [22], [15], [23], [24]. Tumor spheroid growth has been shown to be inhibited due to the application of isotropic compressive stresses. These stresses have a bearing on parameters like packing density and events like apoptosis [16]. Finally, cancer cell lines, in gels of similar mechanical properties as its target organ during metastasis, had correlated cellular responses in terms of proliferation and migration. This provides evidence that cancer cells can detect environmental mechanical properties and initiate unique cellular response depending on them as they travel from their primary tumor site to secondary sites [25].

These examples demonstrate that the cancer tissue and environmental mechanical cues influence cancer behavior at several different scales. Understanding them can greatly complement the traditionally held biochemical perspective of cancer and perhaps in the future offer inputs for therapeutic initiatives.

Hence, it is important to characterize cancer both theoretically and experimentally from a mechanical perspective. To accomplish this, a suitable representative experimental model needs to be chosen. As evidenced from the literature cited previously, a wide variety of models exist from single-cell studies to monolayer cultures and 3D aggregates to xenograft cultures, etc. The 3D aggregates called *Multi-Cultural Tumor Spheroids* (MCTS) are ideal for these experiments because they offer multiple physiologically accurate biological properties, while at the same time being cost-effective and quick to culture

and easy to handle and maintain.

1.3 Multi-Cellular Tumor Spheroids

Multi-Cellular Spheroids (MCS) are three-dimensional spherical cultures of cells. When cultured using tumor cell lines, they are referred to as Multi-Cellular Tumor Spheroids (MCTS). The primary mechanism of MCS formation is due to the formation of bonds between adjacent cells when aggregated together. As cells of a particular cell line aggregate together, the expression of adhesion proteins like cadherin is upregulated. Cadherin is the primary adhesion protein that keeps cells connected to each other. Some studies claim that integrin expression is also altered [26], [27], [28]. When anti-E-cadherin drugs (E-Cadherin is the type Cadherin most used by epithelial cells) are used, compact spheroids from rat hepatocyte cells could not be obtained. [29]. Junction proteins like those of the cadherin family cause the cells to stick together. The expression of additional adhesive proteins like that of gap junctions and pannexins [30] also contribute to the formation of spherical aggregates. Cells inside the MCTS proliferate and increase the overall radius of the aggregate, but the adhesive strength of the junction proteins maintains the cohesion of the entire aggregate. The radii of tumor spheroids have been shown to increase exponentially, followed by a linear region and finally saturates to a constant value [31], [32], [33].

MCS models of tumors and organoids became popular for multiple reasons. Firstly, they exhibit markedly different cell-cell and cell-matrix interactions in comparison to monolayers cultures which was the primary tool for modeling in-vivo systems. These different interactions effect changes in the biochemical and may also affect the bio-physical make-up of the tumor. The effects of these unique cell-cell interactions include enhanced

resistance to radiation, drugs, modulation of protein expression, etc. For example, Chinese Hamster cells could resist higher doses of radiation when cultured in MCS form [34]. The inter-cellular interactions inside MCSs can also activate unique signaling pathways that are not activated in monolayer cultures. For instance, Transcriptional Profiling (TP) of NCI-H1650 and EBC-1 (human lung cancer) cell lines in both 2D and 3D cultures have shown a marked difference in the representation of cell signaling pathways that affect critical cell functions like the cell cycle, angiogenesis, and interleukin activation [35]. Furthermore, both elicited and influenced by these cell-cell interactions are the formation of profound gradients in the distribution of glucose, ions, oxygen and many other metabolites, which in turn introduce bio-chemical (figure 1.3) and potentially biophysical gradients inside the spheroid [36].

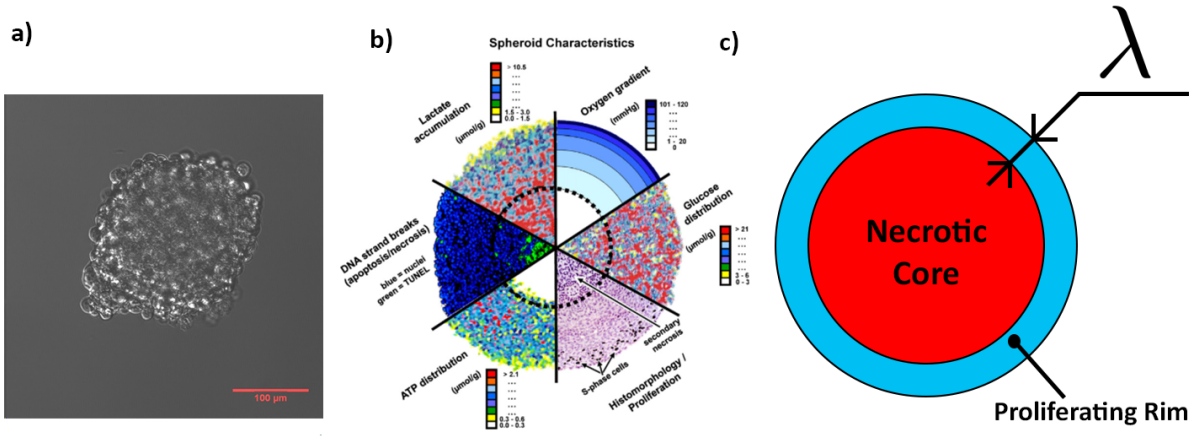

Figure 1.3: a) An MCF10ca1a breast cancer Multi-Cellular Tumor Spheroid (MCTS) cultured via the hanging droplet technique. The thickness of the spheroid is evidenced by the relatively darker regions in the center. b) The many biochemical gradients that are established inside the MCTS [37]. c) A simplified diagram showing the levels of proliferation of cells at different locations inside the MCTS (red represents the necrotic core, while blue represent healthy cells)

Consequently, MCS offers a more holistic and physiologically relevant representation of organs in-vitro [38]. Hence, the medical community has been quick to adopt them as

reliable models that mimic in-vivo systems. Some of the most widely used applications have been to study avascular tumor growth [39].

The majority of previous work on MCTS focus almost exclusively on their biological aspects. However, as explained earlier, large gaps remain when attempting to characterize their behavior. Multiple theoretical models are describing how aggregates grow and invade, but a comprehensive model that explains their behavior continues to remain elusive. Viewing spheroid growth from a mechanical property is a fresh perspective to this age-old problem. Well-thought-out theoretical models of their mechanical behavior will serve to guide experiments and help refine experimental hypothesis in this nascent field which the scientific community is only starting to explore [40]. This thesis aims to explain a continuum model to understand the internal mechanics of tumor aggregates and instabilities that lead to tumor invasion. It particularly examines if a solid-to-fluid phase transition takes place in a growing avascular MCTS that causes it to invade. However, before getting into its details, it is interesting to review some of the popular and widely cited theoretical models that have informed the present study.

1.4 Modeling Multi-Cellular Tumor spheroids

Akin to classifications of theoretical models in many fields of science, the practice of modeling Multi-Cellular Tumor Spheroids can be broadly separated into *continuum*, *discrete* and the relatively recent *hybrid models*. The continuum models approximate that the properties of the tissue system under study vary smoothly and continuously. The characteristic dimensions of the system are much larger than the size of the cells. It is hence appropriate for studying bulk tissue behavior and also reduces computational cost. Discrete theoretical models track the individual behavior of cellular agents, by specify-

ing rules for them and observing emergent behavior of the cell collective. These models are suitable to study cell-cell interactions, but can quickly become computationally unwieldy. Each modeling technique is effective at different length scales and depending on the behavior of interest. Finally, hybrid models attempt to combine both continuum and discrete assumptions to capture tissue behaviors at different length scales (multi-scale modeling of cancer) [41].

Models in these categories vary in complexity - some attempt to understand tumor growth, others invasion, and some others *angiogenesis* - the process by which the tumor recruits blood vessels for itself. However, the present study focuses on the growth of an avascular tumor spheroid using continuum assumptions, its internal mechanics and the mechanical instabilities they form as they invade.

1.4.1 Cancer growth as a Reaction-Diffusion Problem

One of the earliest approached to model tumor growth was to characterize it as a diffusion problem. A spherical symmetry condition would be assumed and molecular gradients - some for nutrient molecules and some for proliferation inhibitors would be introduced. These models could solve for the spheroid radius as a function of time [42]. In the same era, modifying such models by adding a reaction term to the equation was also done commonly. Models such as these were used to derive critical parameters transitions of which lead to instabilities or limitless growth occurs [43] - considering the growing tumor as a dynamical system. Multiple models from this era improved upon the reaction-diffusion scheme to increasing levels of complexity. Some models even took into account the concentrations of over four different ionic species, glucose and oxygen levels and pH levels to model MCTS growth and demonstrated experimental correlations [44].

In addition to capturing nutrient transport, an important leap forward was to model the presence of the necrotic core inside tumors that are caused by cell death due to gradients of nutrients established inside the spheroid [45] (refer figure 1.2)). Finally, models based on the reaction-diffusion approach was also used to include the transport of matrix-degrading enzymes and incorporate cell-ECM interactions and consequently study tumor invasion [46]. These models were able to solve for the distribution of cell nutrients and offer some of the first estimates for the evolution of the spheroid radius. The authors of these pioneering articles highly emphasized the transport of nutrient molecules. They inform that the spheroid and its environment are subject to important property gradients and motivated by this, the present study coarse-grains these effects in the form of mechanical property and cell proliferation gradients.

In the years that followed these models, as explained in section 1.2, as the scientific community began to realize the growing importance of mechanical field variables involved in cancer growth, these reaction-diffusion models began to be coupled with constitutive models. These constitutive models described the variations in shear stresses, normal stresses components and pressure inside and around the spheroid. One of the earliest equations that were used in these models is Darcy‘s law, which was primarily used to model flow a through porous medium.

$$\vec{\boldsymbol{u}} = -\frac{1}{\kappa}\boldsymbol{\nabla} \cdot p\boldsymbol{I}$$

Where κ is an averaged representation of the permeability (hydraulic resistance) of the porous structure. Reaction-Diffusion Models using Darcy's law has been used to simulate tumor invasion. An interesting modification to this model was to use a tissue tension boundary condition at the tumor-medium interface to coarse-grain the effect of intercel-

lular adhesion at the aggregate surface [47], [48].

Another kind of constitutive model is based on the Stokes‘ flow assumption. Here, the MCTS is treated as a fluid and the inertial terms are considered to be small enough that the convective term of the Navier-Stokes equation can be neglected;

$$-\boldsymbol{\nabla} \cdot p\boldsymbol{I} + \mu \boldsymbol{\nabla} \cdot \left[\boldsymbol{\nabla} \vec{\boldsymbol{u}} + (\boldsymbol{\nabla} \vec{\boldsymbol{u}})^T \right] = 0$$

This is applicable because the time scale of cancer cell division and propagation is large enough that inertial influences due to their motion can be neglected. Coupling the continuity equation and the stokes law assumption with a nutrient transport equation has been used to study spheroid growth [49], [50]. There is scarce literature about the use of Stoke's law as a constitutive model, but it has also been used to simulate tumor metastasis [51]. Two-phase models that couple the mass conservation equation with the momentum conservation equation with special source terms and a proliferation gradient dependent on oxygen levels have also been used to simulate tumors [52], [53].

A radically different set of constitutive models is drawn from the family of nonlinear mechanics models. Some of these include poroelastic models such as using Brinkman equations, hyper-elastic models and linear and nonlinear visco-elastic models that attribute stiffness and viscosity via storage and loss moduli. Some authors have also extended these models to the tumor micro-environment, for example, in one model, the tumor spheroid is suspended in a porous medium and the location is determined by defining volume fractions for the solid domain and the fluid domain [54]. Another approach was to model solid tumor growth as a nonlinear elastic material and obtain conditions for metastasis in terms of strain energy functions [55]. Other non-linear approaches in-

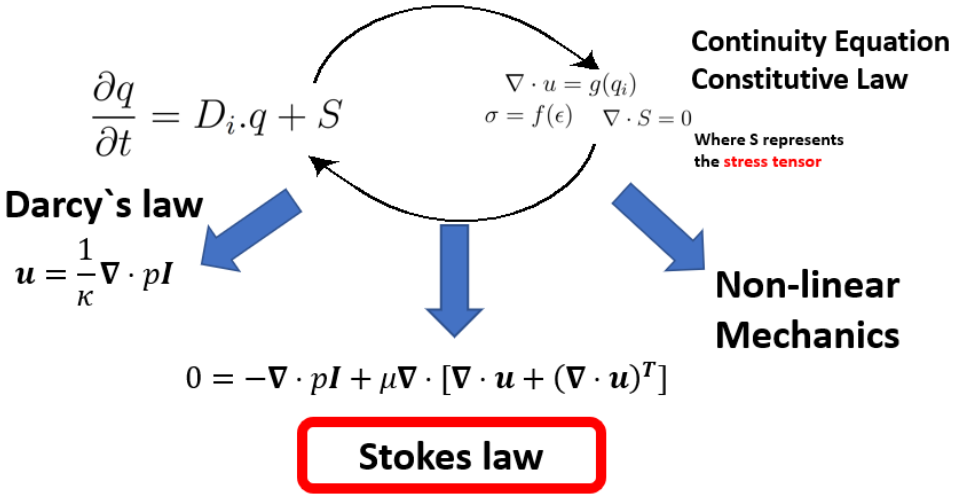

Figure 1.4: Modeling the mechanics of MCTS in the past have been done by coupling reaction-diffusion equations with constitutive laws and the continuity equation. Some examples of popular constitutive laws are Darcy's law, Stokes' law and those derived from nonlinear mechanical models.

clude modeling the deformable micro-environment as a hyper-elastic material [56], [52]. In addition to these well-known material models, formulation of unique constitutive laws which better describe the mechanics of the tumor has been coupled with the mass conservation or the diffusion equation to improve upon the extant models [57]. In almost all these papers, the authors have conducted a linear perturbation analysis to characterize the morphologies associated with growth or invasion as mechanical instabilities. Hence, a similar approach is taken in this study, where parametric sweeps are calculated across multiple scales to study phase transitions that might occur during tumor growth.

These afore-mentioned models only form a small group of large effort towards modeling cancer progression in mechanics. In addition to these models which have reaction-diffusion equations coupled with constitutive models, some other interesting models add further details such as distinguishing the cancer tissue and the micro-environment as different phases such as using Cahn-Hilliard Equations[58], mixture theory [59] and a

variety of other approaches [60]. For reference, the reader can refer the thorough reviews [61], [62], [63], [64].

The present study introduces a continuum mechanics model implemented in COMSOL Multiphysics using a Stoke‘s flow assumption, combining a moving-mesh algorithm based on the Arbitrary Langrangian-Eulerian (ALE) scheme which qualitatively captures morphological changes associated with tumor growth. This is a fluid-fluid interface allows the specification of surface tension between the tumor spheroid and the tumor micro-environment. The model in Chapter 2 simulates the tumor spheroid in using a 2D axisymmetric model. This model coarse-grains the effect of the afore-mentioned nutrient profiles that are established in an MCTS. This is achieved by implementing a gradient in viscosity and cell proliferation. The cells in the core are deprived of critical nutrients needed for their survival and are undergoing necrosis. Hence, the organized structure they form is rigid and they can be modeled as a fluid with a large time scale and hence a large viscosity. In contrast, the rim of outer cells are rich in nutrients and proliferate actively. They are not fixed in place and are free to move and they can be modeled as fluid with small time scales or low viscosity. Imposing these profiles represent a solid-to-fluid phase transition from the center of the spheroid to the outer rim. This chapter isolates this effect which is starting to be seen in different biological systems [9] and confirms if it initiates tumor invasion via surface instabilities.

In chapter 3, cancer growth in a 2D planar model is simulated. Here, the instabilities that are formed due to both proliferation and curvature dependent normal active stresses are considered. The same profile of viscosity is implemented and the effect of the active stresses and proliferation on tumor invasion is investigated. The commercial solver package COMSOL Multiphysics (5.3) and (5.4) along with MATLAB is used to implement the

model explained in both chapters to calculate the mechanical profiles inside the spheroid and to investigate instabilities caused by growth and active stresses. Further, in chapter 4, a summary of the experimental techniques - from sample preparation to the last data analysis step is explained, followed by a concluding chapter and discussions on potential future work in this area.

Chapter 2

Two-phase Axisymetric Model of Tumor Growth

2.1 Introduction

Tumor invasion can be compared to multiple physical phenomena found in nature. Considering the spherical arrangement of cells from a mechanical perspective, the continuous growth of the spheroid can introduce surface instabilities to compensate for the increased surface area. These instabilities could facilitate tumor invasion as they are finger-like and offer an invasive morphology for the cells as they attempt to escape the primary tumor site. Analogous to a system with a source enclosed, a decrease in the surface tension, which contains the growth can lead to instabilities of this nature. However, like changes in the surface properties, changes in the bulk of the tumor are equally important. The gradients of nutrients and other properties that arise inside the 3D spheroid could give rise to mechanical gradients - particularly one in viscosity as the cells in the proliferative region are more motile than those in the necrotic core. Further, when the tumor invades, the solid tumor could potentially undergo a fluidization process to release

cells that invade the tumor surroundings. Consequently, it may be hypothesized that the invasion of the spheroid is due to a solid-to-fluid phase transition.

To test this hypothesis, this chapter begins with a simple model consisting of incompressible Newtonian fluid domains - the spheroid and the micro-environment having a distinct boundary in a 2D axisymmetric geometry. The Stokes law assumption of neglecting inertial terms in the Navier-Stokes Equation has been implemented. The chapter describes the computational domain, the governing differential equations, the relevant scales of the problem and finally a discussion of the results.

2.2 The Arbitrary Lagrangian-Eulerian Algorithm

Much academic effort has been dedicated to understanding the growth of tumors using a multi-phase fluid approach. As exemplified in the previous chapter, several scientists [53], [64] have considered the tumor and its micro-environments as distinct domains and captured the interface using phase-fields or level-set approaches. However, these are diffuse interface techniques and computationally quite expensive. This chapter explains how the two-phase moving mesh module in COMSOL Multiphysics can be used to describe the growth of tumor spheroids. A range of parameter regimes is investigated to predict mechanical instabilities that can elicit cancer invasion using COMSOL's in-built Parametric Sweep option. Briefly, the two-phase moving mesh physics module is one of the many methods that COMSOL offers for interface capturing. It uses the Arbitrary Lagrangian-Eulerian (ALE) algorithm for coupling the fluid flow with mesh deformation and hence can simulate moving boundaries. The following sections describe the governing equations solved for, the material properties imposed and the results from

the simulations.

The Lagrangian approach of solving finite element problems involves the use of a deformable mesh. The deformable mesh permits the tracking of a control volume as it moves through the computational domain. The observer's frame is the same as that of the control volume. In the Eulerian approach, the mesh is fixed and does not follow the control volumes as they move. The observer's frame is fixed and does not change.

The Arbitrary Lagrangian-Eulerian algorithm makes use of both these classical representations of Finite Element Methods. It makes use of a mapping from a deformed (Lagrangian) mesh to that of a simpler, ordered mesh (Eulerian). The mapping is smooth and one-to-one.

Specifically, the governing differential equations that are solved in the moving-mesh domain is transformed using the aforementioned mapping into the simpler domain. Here, the transformed equations are solved using an additional term containing information about the mesh velocity. This new equation is solved and the solutions are mapped back into the deformed domain.

2.3 Governing Differential Equations

The governing differential equations consist of the Continuity Equation (2.1) and the incompressible Stokes (2.2) applied on both domains (tumor spheroid and environment). The continuity equation has a source term (on RHS) that represents cell division and consequently regulating the proliferation. Hence, the equations solved for the tumor aggregate (domain - I) are;

$$\rho \boldsymbol{\nabla} \cdot \boldsymbol{u_1} = G(r, z) \tag{2.1}$$

$$-\boldsymbol{\nabla} \cdot p_2 \boldsymbol{I} + \mu(\boldsymbol{x}) \boldsymbol{\nabla} \cdot \left[\boldsymbol{\nabla} \boldsymbol{u_1} + (\boldsymbol{\nabla} \boldsymbol{u_1})^T - \frac{2}{3} \boldsymbol{\nabla} \cdot \boldsymbol{u_1} \right] = 0 \tag{2.2}$$

Similarly, the tumor spheroid is suspended in a cylindrical domain. The boundary conditions of the micro-environment (domain II) includes an outlet condition on the far edge and two wall conditions on the top and the bottom. The micro-environment is modeled as an incompressible Newtonian fluid with properties that of water, but a smaller viscosity than that found inside the spheroid. The equations solved are;

$$\boldsymbol{\nabla} \cdot \boldsymbol{u_2} = 0 \tag{2.3}$$

$$-\boldsymbol{\nabla} \cdot p_2 \boldsymbol{I} + \mu_2 \boldsymbol{\nabla} \cdot \left[\boldsymbol{\nabla} \boldsymbol{u_2} + (\boldsymbol{\nabla} \boldsymbol{u_2})^T \right] = 0 \tag{2.4}$$

These are subject to the boundary conditions related to the interface between the tumor

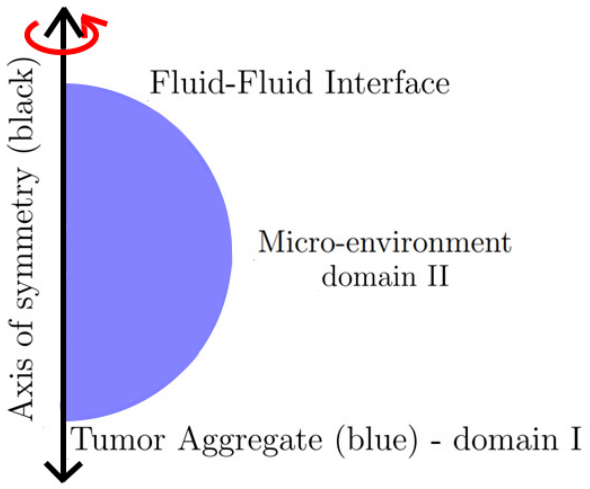

Figure 2.1: 2D axisymmetric geometry of the Spheroid (blue) suspended in a Newtonian fluid Medium

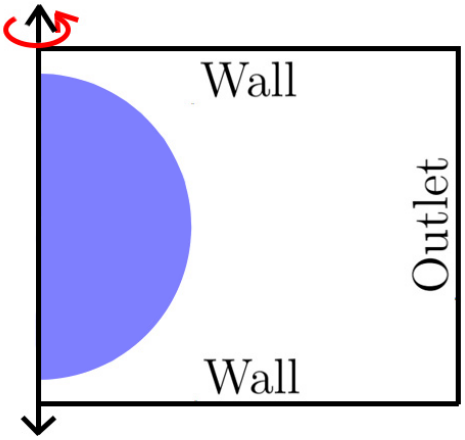

Figure 2.2: Boundary Conditions of the Tumor Micro-environment - Wall and Outlet boundary conditions. The interface between the spheroid and the domain is modeled using the Young-Laplace interfacial tension Condition

and tumor micro-environment;

$$n_j(\sigma_{ij}^{(1)} - \sigma_{ij}^{(2)}) = \gamma(\nabla \cdot \hat{\boldsymbol{n}})n_i$$

where

$$\sigma_{ij} = -p\delta_{ij} + \mu(\boldsymbol{x}, \lambda)\dot{\epsilon}_{ij}$$

γ is the coefficient of interfacial tension and $\hat{n}$ is the unit outward normal. Constant pressure outlet conditions $p_2 = 0$ and no-slip wall conditions $u_2 = 0$, as specified in figure 2.2.

2.4 Computational Domain

The computational domain is modeled in a 3-D axisymmetric geometry mode. This is a technique used by COMSOL to take advantage of the symmetry of the problem and hence reduce computational time. The coordinates are specified using cylindrical coordinates (r, z). Hence, a fully revolved rendering represents a spherical tumor spheroid

suspended in a cylindrical domain filled with media.

The initial radius of the tumor spheroid is $100\mu m$. The micro-environment surrounding it is made 150 times larger with a radius and height of $15mm$. It is made large so that the wall conditions do not influence the growth of the spheroid inside an incompressible, Newtonian fluid medium.

2.5 Relevant Dimensionless Parameters

We use the cell division time τ and the length of proliferation zone λ as the characteristic time and length scales in the problem. Using this characteristic length and time scale, two dimensionless numbers; the Capillary Number (Ca) and the ratio of the shear stress in the proliferating rim to the shear stress in the necrotic core. These two dimensionless numbers dictate the solutions of the system. The Capillary number is defined as;

$$Ca = \frac{\sigma_c}{\sigma_s} = \frac{\tau\gamma}{\mu_c\lambda}$$

Where γ is the co-efficient of interfacial tension between the tumor spheroid and its micro-environment and μ_c is the viscosity of the necrotic core region of the spheroid. The other dimensionless number β is defined as

$$\beta = \frac{\sigma_f}{\sigma_s} = \frac{\mu_f\tau}{\mu_s\tau}$$

Where, μ_r is the viscosity in the fluidized proliferation rim and σ_f is its associated shear stress. σ_S is the shear stress in the necrotic core region and μ_s is the viscosity.

2.6 Material Properties

As seen in equation (2.1) and (2.2), the proliferation G and the viscosity μ are both functions of position inside the moving domains. To apply these property variations, the general extrusion operator along with the piecewise function and variable definition in COMSOL has been used.

2.6.1 Defining a distance operator - d_R

The general extrusion operator represents a transformation of geometry from a lower dimension to a higher dimension. For instance, with the appropriate settings, it allows the extraction of property value from an arc and assigns it to a surface. In this case, the general extrusion tool has been used to design a distance field from the moving boundary.

The method to accomplish this is to select the desired arc geometry elements of the tumor in the general extrusion settings interface. The Destination Map fields are specified as r and z in their respective fields and in the advanced tab, the Mesh Search Method is changed to the closest point. Next, a variable is defined which computes the distance and is assigned the following formula. If the general extrusion operator is named A_b

$$d_R(r,z) = \sqrt{(r - A_b(r))^2 + (z - A_b(z))^2}$$

Which defines a distance operator for each point (r, z) from the contour of the spheroid The distance operator is used as an argument for a piece-wise function that chooses the value of the material property. This allows the model to assign material properties based on the distance from the boundary.

2.6.2 Material Property profiles of the Tumor Aggregate

Tumor aggregates in this model have been idealized as perfectly spherical initially. They are termed spheroids of tumor cells. The formation of spheroids is physiologically possible as evident from a variety of in-vitro and in-vivo techniques.

Three-dimensional cultures of tumor cells offer more accurate models of studying them via drug perturbations from both a biochemical and biophysical perspective [35]. This is justified by their ability to form physiologically relevant gradients in nutrients levels, oxygen concentration, ions, and other chemical species. The primary reason for these gradients being their inability to diffuse into the spheroid core.

These gradients have significant consequences. Multiple articles mentioned in chapter 1 including the earliest models relying solely on diffusion [42], [43] have paid careful attention to them while modeling tumor spheroid growth. However, the model presented does not address the transport of these chemical species but represent their consequences in terms of material property profiles. Two such property profiles resulting from these gradients are step-function like variations in proliferative capacities of the cells and dynamic viscosities. To implement these in COMSOL, two piece-wise functions are defined, one for proliferation and another for viscosity.

$$\mu(r,z) = \begin{cases} \mu_r & d_R(r,z) \leq \lambda \\ \mu_s & d_R(r,z) > \lambda \end{cases}$$

Where μ_r represents the viscosity in the proliferating rim of the tumor spheroid and μ_s is the viscosity in the necrotic core of the spheroid. λ is the thickness of the proliferating shell of cells around the necrotic core of the spheroid. To be physiologically accurate, the

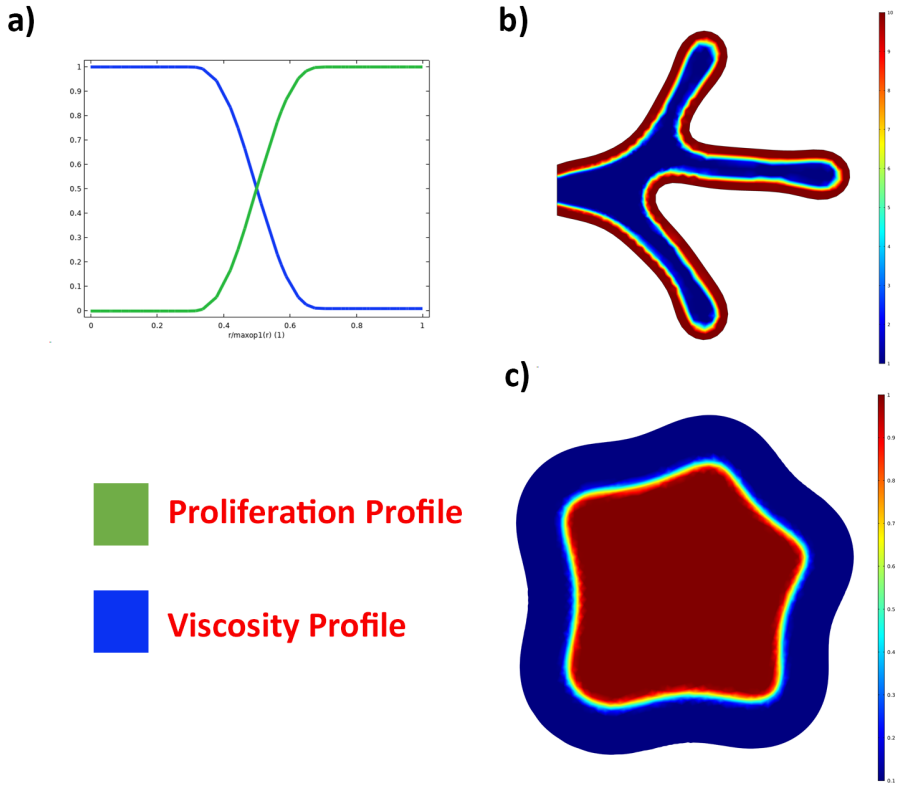

Figure 2.3: a) Functions showing the transition of proliferation rate and viscosity from the necrotic core region to the proliferating rim. It is required to prevent potential singularities in the system. b) Application of the piece-wise function ($G(r,z)$ and $\mu(r,z)$)to set up the proliferation and viscosity gradients in the axisymmetric geometry The function can follow the curvature of the spheroid and applies the properties as a function of distance from the envelope. c) The application of the gradients in a 2D planar geometry via the piece-wise functions.

region between the proliferating domain and the necrotic core is occupied by quiescent cells, but an explicit description of them have been left out in this study. The proliferation rate is also similarly defined using the general extrusion operator and the distance function;

$$G(r,z) = \begin{cases} G & d_R(r,z) \leq \lambda \\ 0 & d_R(r,z) > \lambda \end{cases}$$

Where G is a constant specified in the global parameter definition of COMSOL and is defined as $G = \frac{\rho}{\tau}$, where ρ is the density of water. This definition states that the proliferative rim is constantly dividing and that the necrotic core is not undergoing cell division. To avoid numerical problems arising from discontinuities, the piece-wise functions are smoothed between the two-step values by a function that has a continuous second derivative across a transition zone of 0.4λ.

The boundary between the tumor spheroid and the tumor micro-environment has been explicitly modeled using a fluid-fluid interface node in COMSOL. This node makes it possible to specify both the direction, mass flux and the magnitude of the interfacial tension at the tumor-tumor microenvironment interface. In the present model, only the coefficient of the interfacial tension is specified without a mass flux across the interface.

In addition to the material properties imposed in this fashion, the remaining properties, such as density, compressibility, etc. of both domains are assumed to be that of water at 25^oC.

2.6.3 Material Properties of the Tumor Micro-environment

As previously mentioned, the tumor micro-environment is modeled as an incompressible Newtonian fluid with a lower viscosity than that found inside the spheroid. The viscosity steps are calculated by multiplying the shear stresses in the spheroid by the characteristic time constant τ. The shear stresses are assigned based on the ratio of the rim to necrotic core viscosities β which is swept using COMSOL's parametric sweep. The viscosity of the micro-environment was held constant at a value much lower than the viscosity of the necrotic core.

2.7 Scaling the Governing Differential Equations

Using the physical parameters described in the previous sections, the governing differential equations (2.1) through (2.4) can be scaled as follows;

$$\rho\frac{\tilde{\boldsymbol{\nabla}}}{\lambda}\cdot\frac{\tilde{\boldsymbol{u}}_{\mathbf{1}}\lambda}{\tau}=G(r,z)$$

$$\implies \tilde{\boldsymbol{\nabla}}\cdot\tilde{\boldsymbol{u}}_{\mathbf{1}}=\frac{G(r,z)\tau}{\rho} \tag{2.5}$$

$$-\frac{\tilde{\boldsymbol{\nabla}}\cdot\tilde{p}_1\boldsymbol{I}}{\lambda}\sigma_s+\mu(r,z)\frac{\tilde{\boldsymbol{\nabla}}}{\lambda}\cdot\left[\frac{\tilde{\boldsymbol{\nabla}}}{\lambda}\frac{\tilde{\boldsymbol{u}}_{\mathbf{1}}\lambda}{\tau}+\left(\frac{\tilde{\boldsymbol{\nabla}}}{\lambda}\frac{\tilde{\boldsymbol{u}}_{\mathbf{1}}\lambda}{\tau}\right)^T-\frac{2}{3}\frac{\tilde{\boldsymbol{\nabla}}}{\lambda}\cdot\tilde{\boldsymbol{u}}_{\mathbf{1}}\frac{\lambda}{\tau}\right]=0$$

$$\implies -\frac{\tilde{\boldsymbol{\nabla}}\cdot\tilde{p}_1\boldsymbol{I}}{\lambda}+\frac{\mu(r,z)}{\tau\sigma_s}\frac{\tilde{\boldsymbol{\nabla}}}{\lambda}\cdot\left[\tilde{\boldsymbol{\nabla}}\tilde{\boldsymbol{u}}_{\mathbf{1}}+(\tilde{\boldsymbol{\nabla}}\tilde{\boldsymbol{u}}_{\mathbf{1}})^T-\frac{2}{3}\tilde{\boldsymbol{\nabla}}\cdot\tilde{\boldsymbol{u}}_{\mathbf{1}}\right]=0$$

Scaling the viscosity using the viscosity in the necrotic core, we obtain;

$$\implies -\tilde{\boldsymbol{\nabla}}\cdot\tilde{p}_1\boldsymbol{I}+\tilde{\mu}(r,z)\tilde{\boldsymbol{\nabla}}\cdot\left[\tilde{\boldsymbol{\nabla}}\tilde{\boldsymbol{u}}_{\mathbf{1}}+(\tilde{\boldsymbol{\nabla}}\tilde{\boldsymbol{u}}_{\mathbf{1}})^T-\frac{2}{3}\tilde{\boldsymbol{\nabla}}\cdot\tilde{\boldsymbol{u}}_{\mathbf{1}}\right]=0 \tag{2.6}$$

Where

$$\tilde{\mu}(r,z)=\begin{cases}\frac{\mu_r}{\mu_s}=\beta & d_R(r,z)\leq\lambda\\ \frac{\mu_s}{\mu_s}=1 & d_R(r,z)>\lambda\end{cases}$$

Subject to the boundary conditions at the fluid-fluid interface.

$$\implies n_j({\sigma_{ij}}^{(1)}-{\sigma_{ij}}^{(2)})=\gamma(\boldsymbol{\nabla}\cdot\hat{\boldsymbol{n}})n_i$$

Where γ is the coefficient for interfacial tension, σ_{ij} is the stress tensor in domains (1) and (2), $\hat{n}_i$ is the unit outward normal. This is expression can be scaled again with the shear stress in the necrotic core region σ_s;

$$\implies n_j(\tilde{\sigma}_{ij}^{(1)} - \tilde{\sigma}_{ij}^{(2)}) = \gamma\left(\frac{\tilde{\boldsymbol{\nabla}}}{\lambda\sigma_s} \cdot \hat{\boldsymbol{n}}\right) n_i$$

$$\implies n_j(\tilde{\sigma}_{ij}^{(1)} - \tilde{\sigma}_{ij}^{(2)}) = Ca\left(\tilde{\boldsymbol{\nabla}} \cdot \hat{\boldsymbol{n}}\right) n_i \tag{2.7}$$

At the outlet, a constant pressure boundary condition is imposed;

$$\tilde{p}_2 = 0 \tag{2.8}$$

and a no-slip boundary condition at the walls;

$$\tilde{\boldsymbol{u}}_{\mathbf{2}} = 0 \tag{2.9}$$

Equations (2.5) through (2.9) represents the scaled governing differential equations of the system.

2.8 Implementing the Parametric Sweep

The parametric sweep study option in COMSOL is meant to facilitate iterative design and optimization of models. It allows COMSOL to solve the same study after varying one or more parameters of the system. In this case, the parameters swept are the Capillary number Ca and the ratio of the rim to necrotic core viscosities β. These parameters are

varied logarithmically - Ca from 0.01 to 10 and β from 0.01 to 10 and the results of the simulation are shown in the subsequent section. In terms of physical parameters, for each study, COMSOL calculates the viscosities in the system as;

$$\mu_s = \sigma_s \tau$$

$$\mu_r = \sigma_s \tau \beta$$

Here, μ_s is held constant at $10^5 Pas$ and consequently, σ_s is also constant throughout the sweep. The co-efficient of inter-facial tension as;

$$\gamma = \sigma_s \lambda Ca$$

2.9 Results

The parametric sweep explores the parameter space specified by the following table - effectively exploring a wide range of combinations of the Capillary number and the ratio of rim to necrotic core viscosities and the following section details the results obtained from each parameter in the form of relevant field variables such as pressure, velocity, strain rate magnitude, and contour evolution as a function of time. The strain rate magnitude is defined as;

$$\dot{\epsilon} = \sqrt{2\boldsymbol{S} : \boldsymbol{S}}$$

where $\boldsymbol{S}$ is the strain rate tensor $\boldsymbol{\nabla} \cdot \boldsymbol{u} + (\boldsymbol{\nabla} \cdot \boldsymbol{u})^T$ and : is a contraction operator defined such that;

$$\boldsymbol{a} : \boldsymbol{b} = \sum_n \sum_m a_{nm} b_{nm}$$

The results calculated - the mechanical field variables - pressure, shear rate magnitude and velocity magnitude from each of the parameter datasets, for the last time step, considered are shown in the figures below. Additionally, although the variables appear invariant in the cases for $\beta = 1$, there are important profiles here as demonstrated by the radial plot figures. Finally, the evolution of the spheroid contour as time progresses has been shown in figure (2.6).

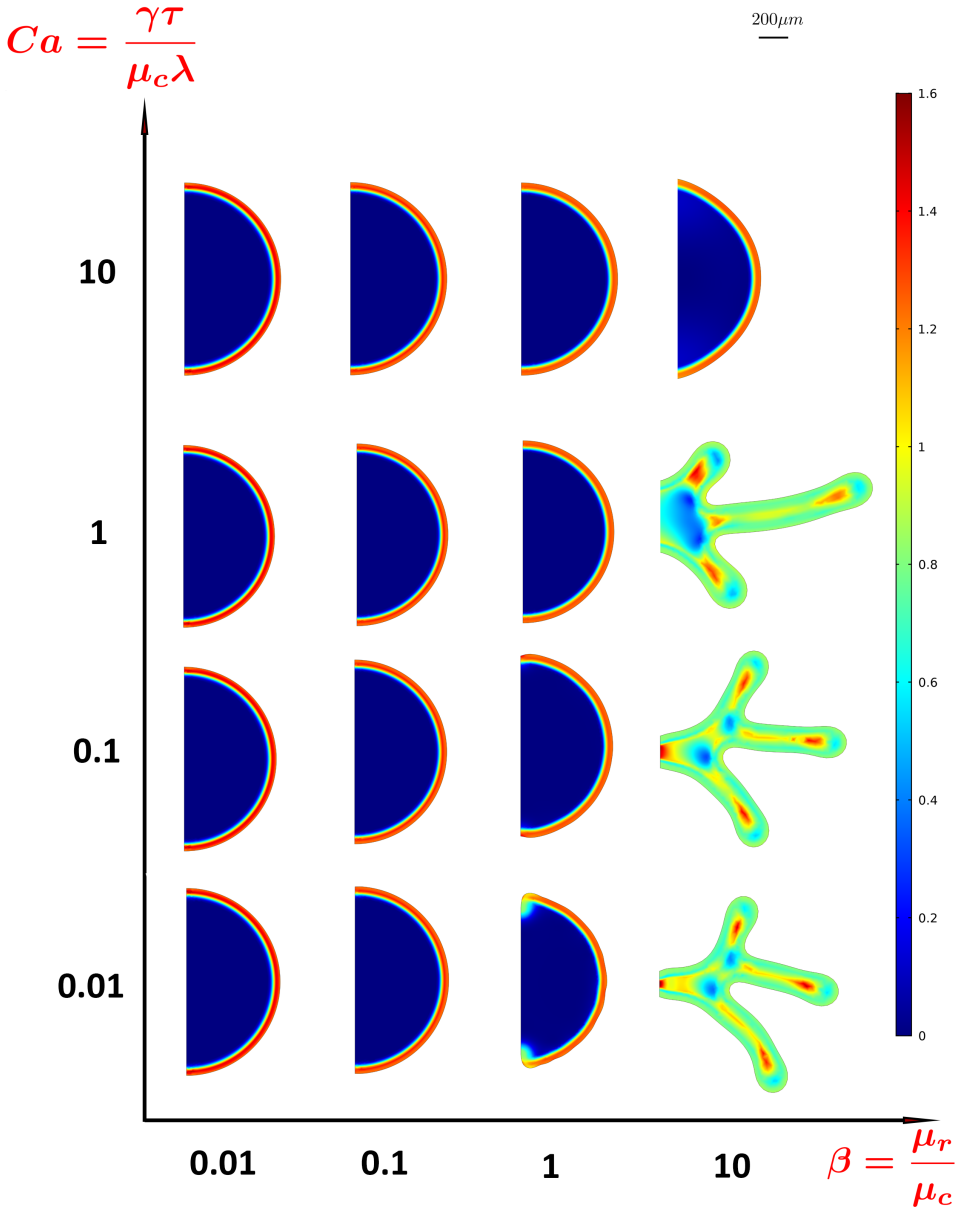

Figure 2.4: Non-dimensionlized Shear Rate Magnitude for different parameter regimes normalized with the characteristic time constant (τ, $\tilde{\dot{\epsilon}} = \dot{\epsilon}\tau$) after 12 time constants of growth, simulated for parameter ranges - β: $(0.01, 0.1, 1, 10)$ and Ca: $(0.01, 0.1, 1, 10)$.

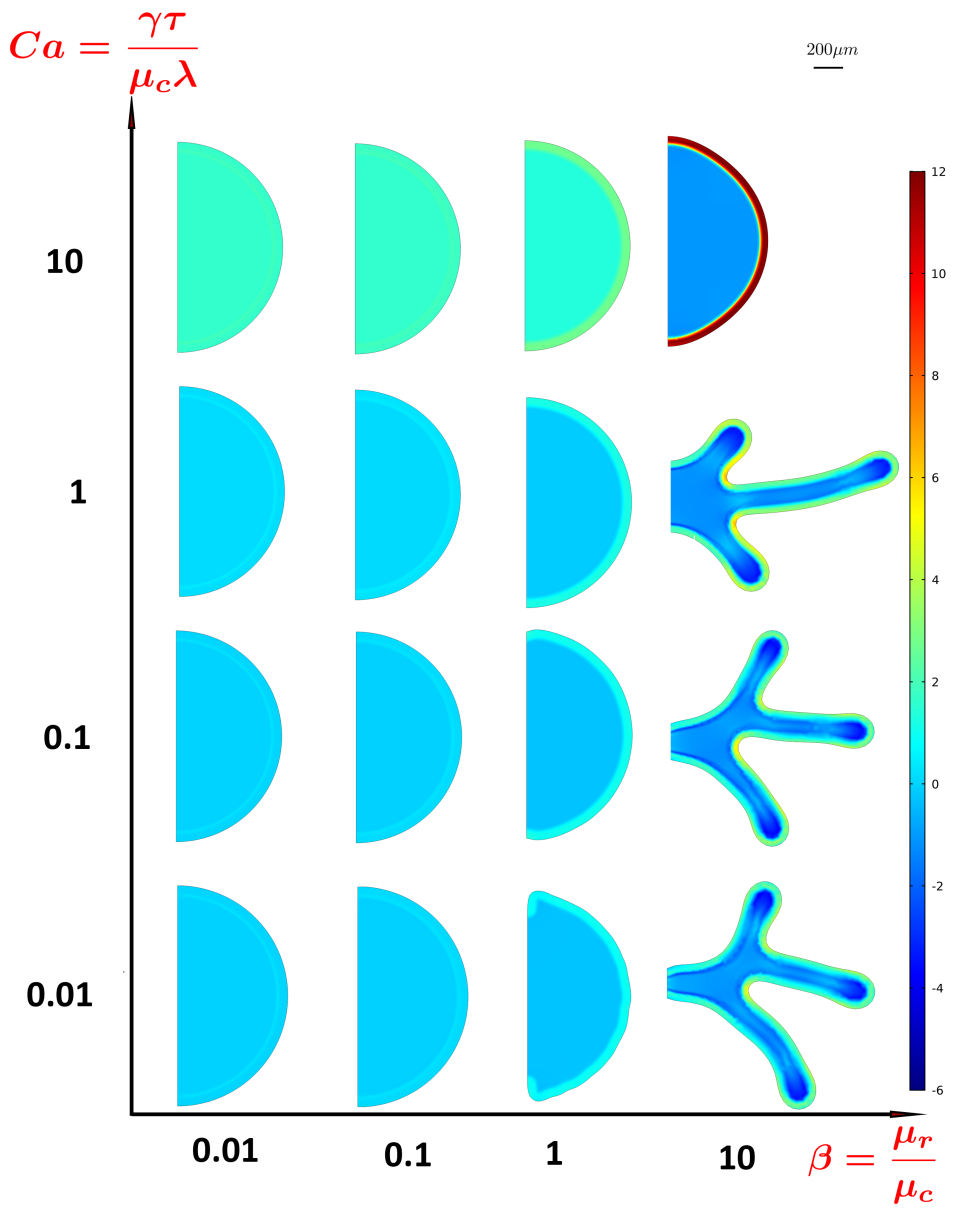

Figure 2.5: Non-dimensionlized Pressure profiles for different parameter regimes normalized with the necrotic core shear stress (σ_s, $\tilde{p} = \frac{p}{\sigma_s}$) after 12 time constants of growth, simulated for parameter ranges - β: $(0.01, 0.1, 1, 10)$ and Ca: $(0.01, 0.1, 1, 10)$.

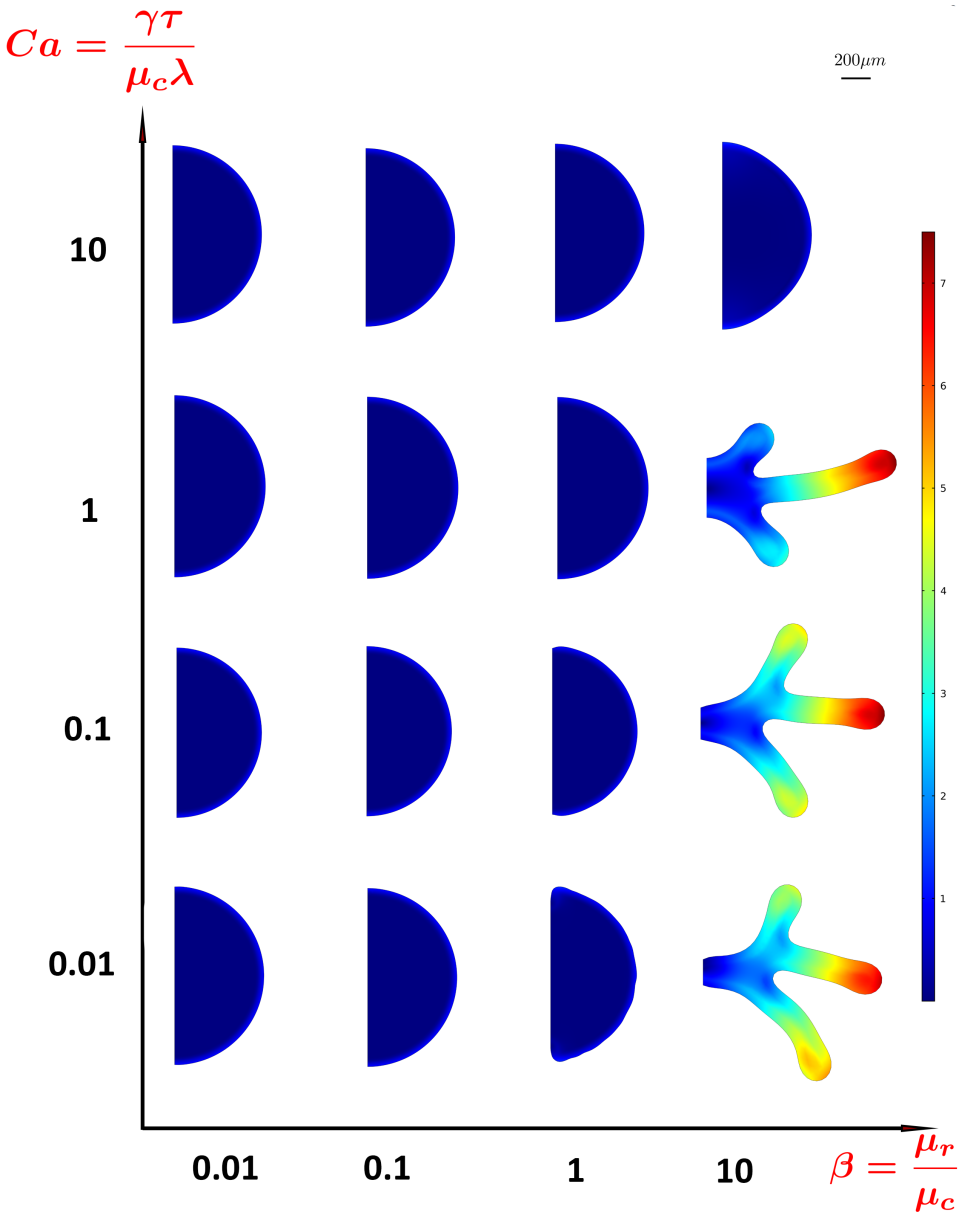

Figure 2.6: Non-dimensionlized Velocity Magnitude for different parameter regimes normalized with the system's characteristic velocity ($\tilde{U} = \frac{\lambda}{\tau}$) after 12 time constants of growth, simulated for parameter ranges - β: $(0.01, 0.1, 1, 10)$ and Ca: $(0.01, 0.1, 1, 10)$.

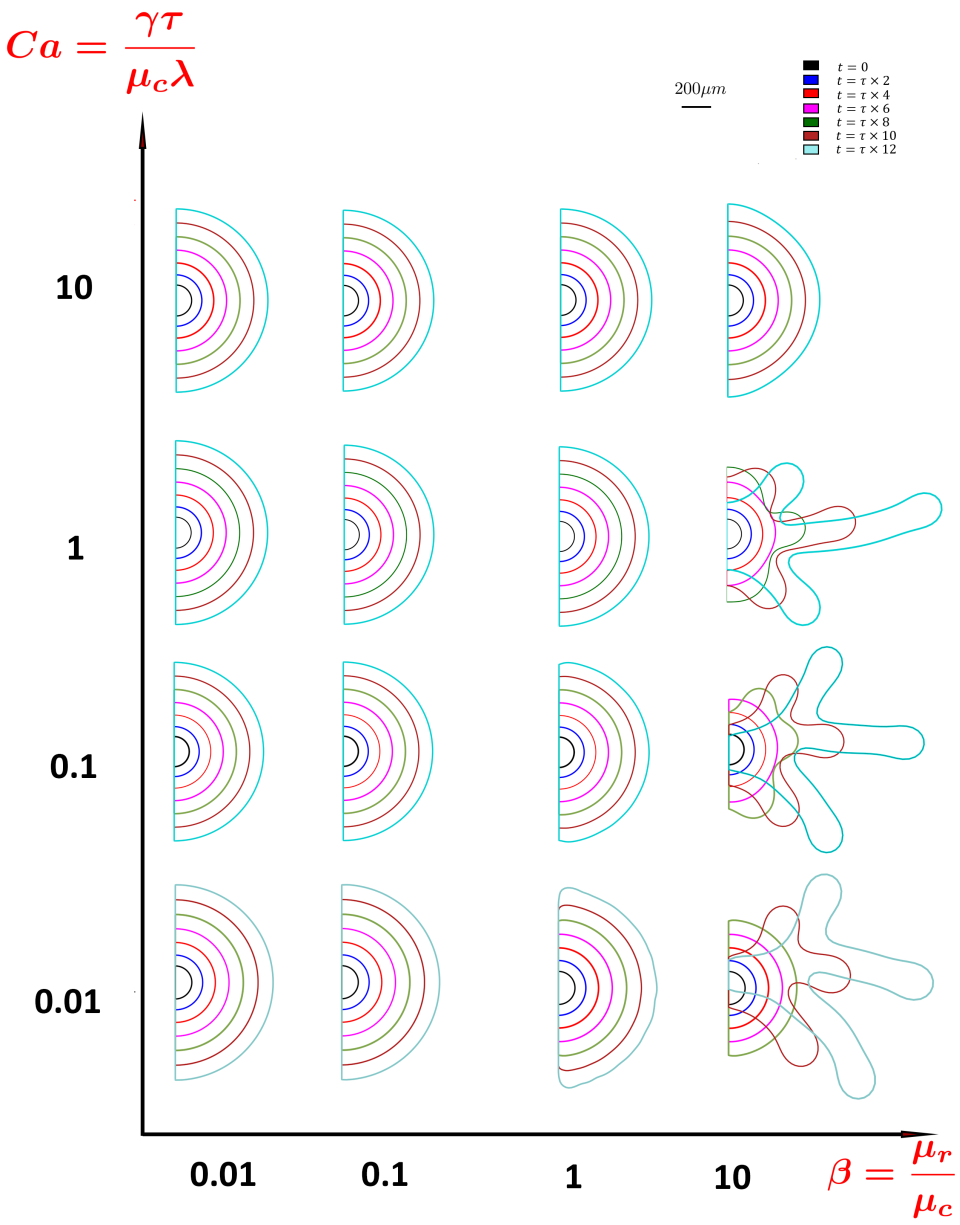

Figure 2.7: Evolution of the Spheroid Contour at every 2τ time step from the simulation

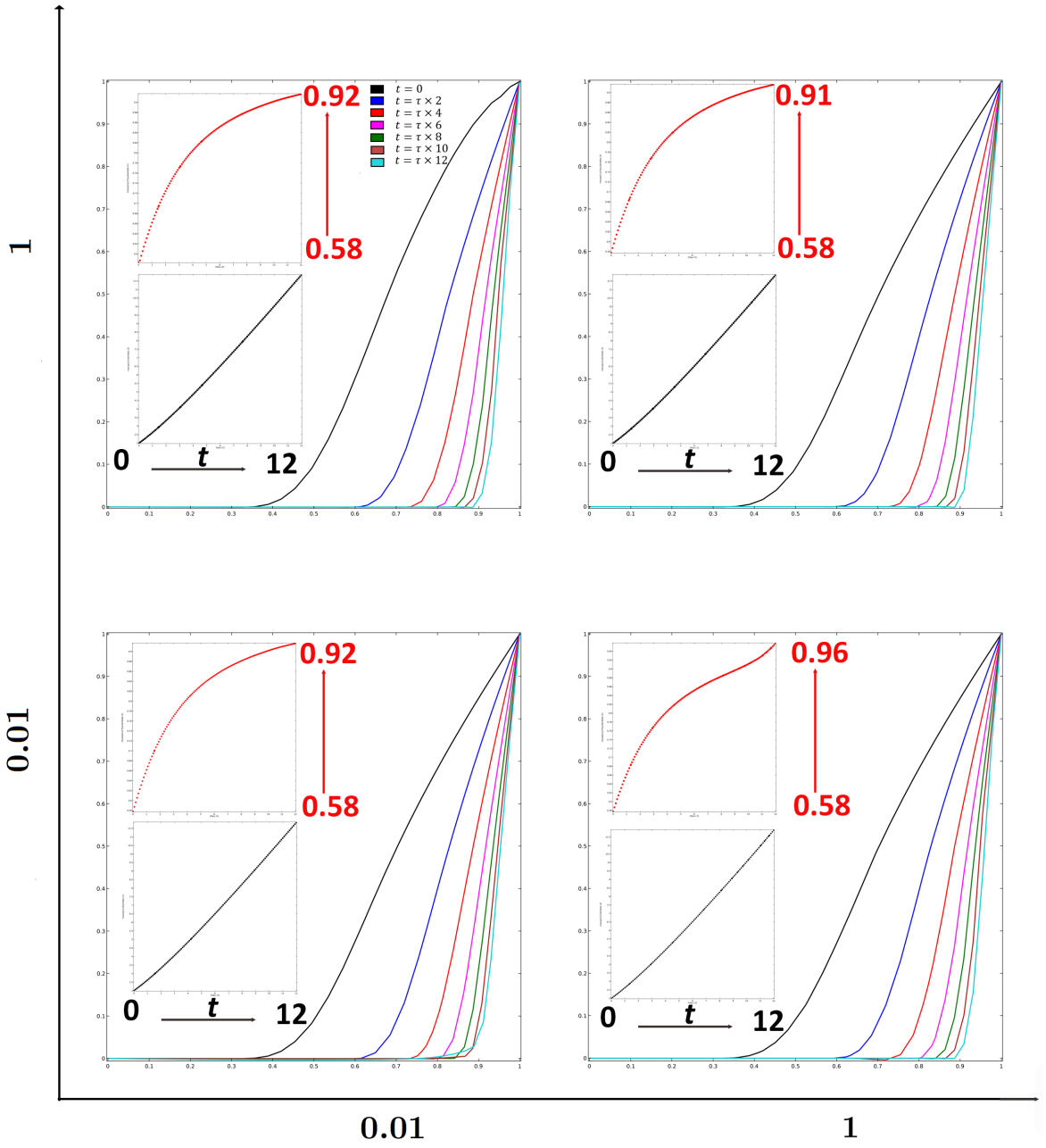

Figure 2.8: The normalized variation (between 0 and 1) of the radial component of velocity along (normalized with the maximum value of velocity along the radius) the radius of the spheroid at intervals of 2 time constants.

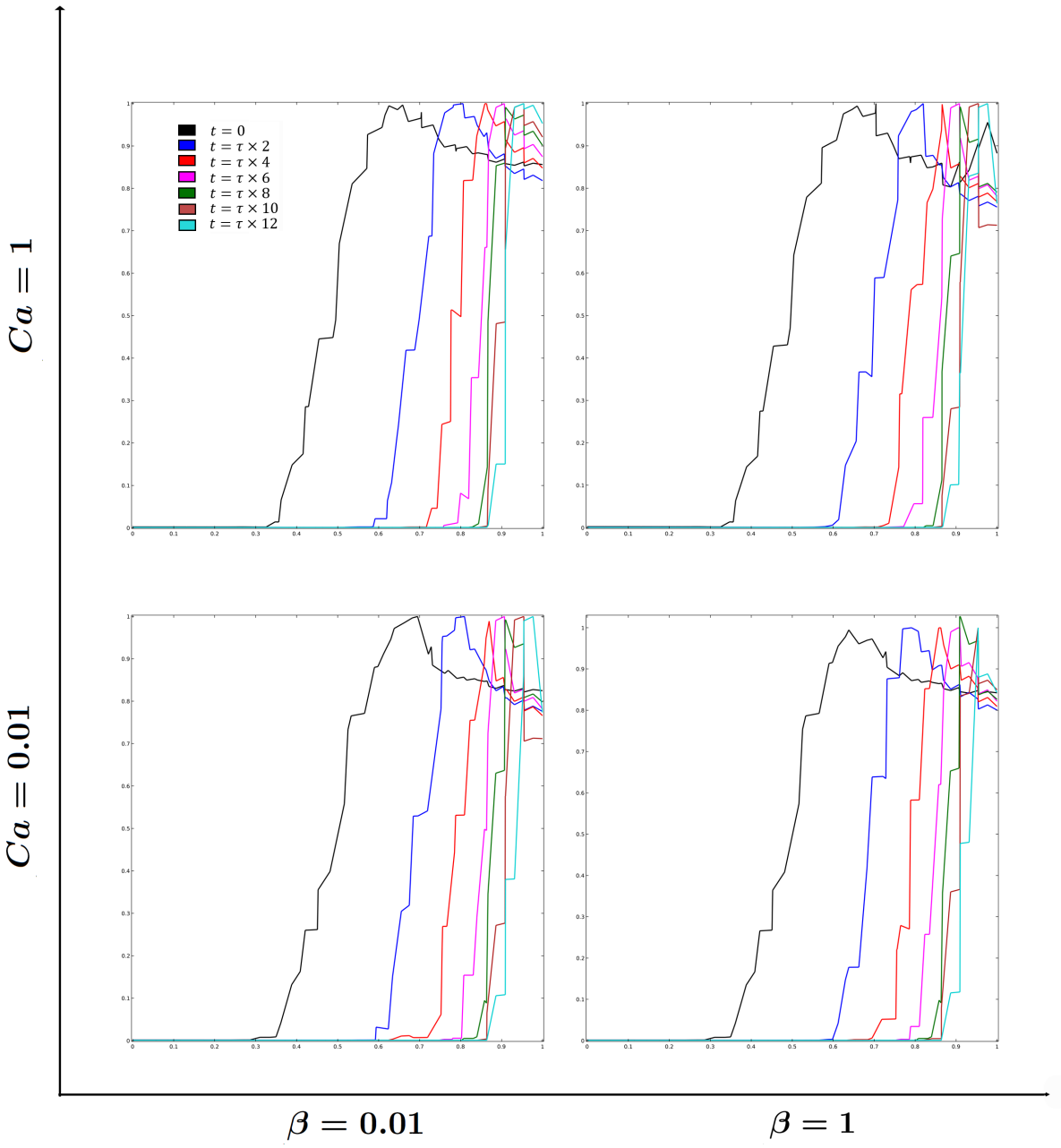

Figure 2.9: The normalized variation (between 0 and 1) of the shear strain rate along the radius (normalized with the maximum value of shear strain rate along the radius) of the spheroid at intervals of 2 time constants.

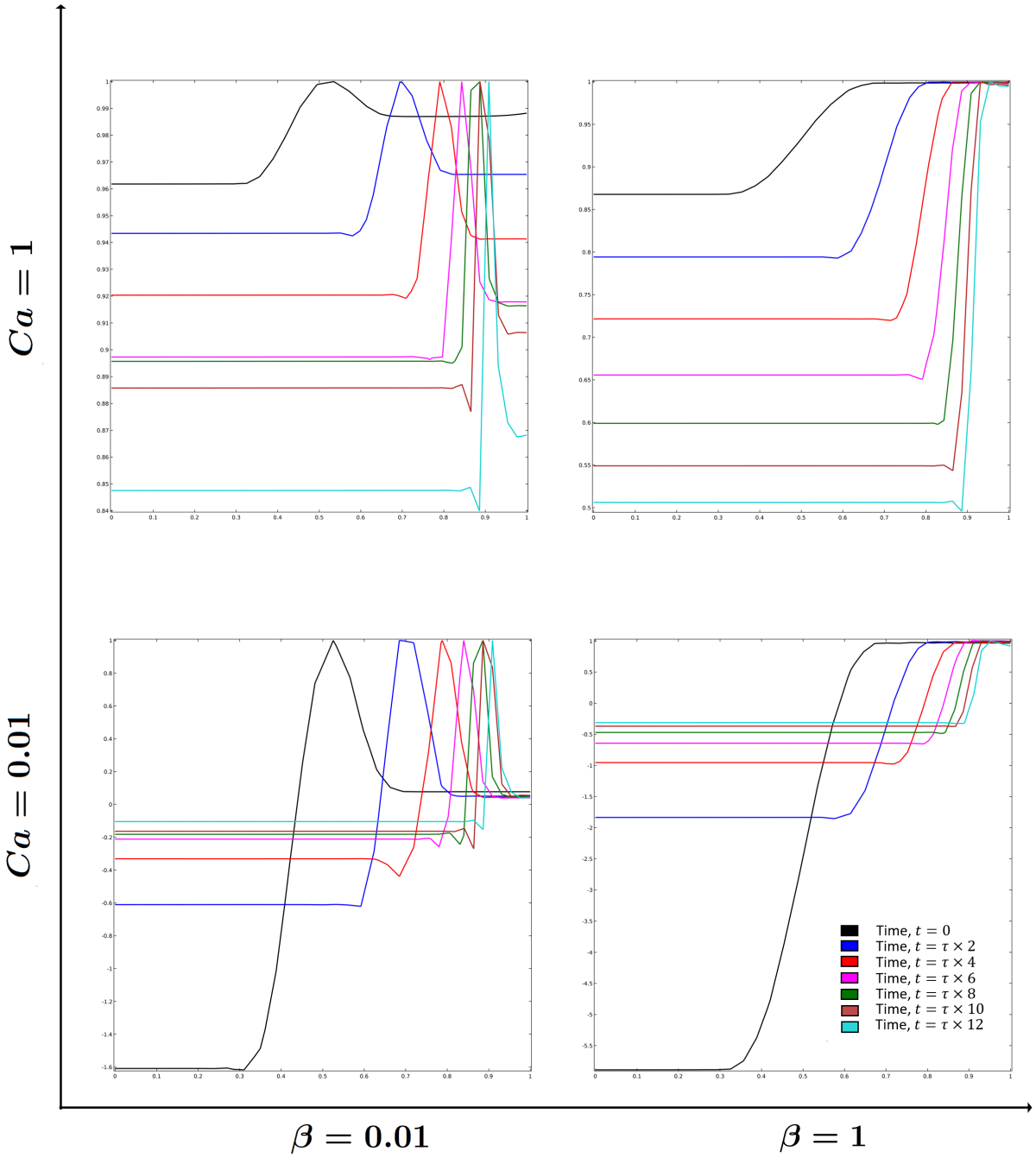

Figure 2.10: The normalized variation (between 0 and 1) of the pressure along the radius (normalized with the maximum value of pressure along the radius) of the spheroid at intervals of 2 time constants.

2.10 Discussion

The simulations solve for the mechanics of a simple coarse-grained model of a spherical colony of cells or an MCTS. This model serves as an initial guess to decide what additional phenomena need to be included. It focuses on the changes in the internal mechanical properties of the tumor spheroid - chiefly the profiles in cell proliferation and viscosity gradients. As the dimensionless parameters that control these internal gradients and the surface properties are varied from one limiting case to another, several interesting phenomena can be observed.

Before moving forward, it is useful to explain how the surface instabilities observed in the results are formed. The boundary condition of interfacial tension between the spheroid and the micro-environment is specified via a co-efficient of surface tension. The Capillary stress is equal to the discontinuity between the states of stress across the boundary. It represents maximum tensile stress the boundary can sustain. The phenomenon can be compared to buckling observed under compressive loading of a pillar. When compressive stresses exceed the critical compressive load, the pillar buckles. Similarly, when the fluid shear stress in the spheroid exceeds the capillary stress, the ratio of viscosities β and the proliferation rate of the cells becomes the driving force that dictates the morphology of the spheroid. These need to be contrasted with numerical instabilities that, due to the expanding domain size, appear like mechanical instabilities due to insufficient meshing. When the mesh is refined sufficiently, these numerical instabilities will disappear. Further, the presence of the axial boundary condition in the 2D axisymmetric case could also influence these instabilities, which is why to eliminate this possibility, further models are simulated using a fully 2D geometry.

According to figure 2.1, the buckling instabilities are evident for a value of $\beta = 10$. This is because the shear fluid shear stresses are much higher than the Capillary stresses and the inner region of the tumor aggregate is much less viscous compared to the proliferative rim. However, according to the explanation given in the previous paragraph, the instabilities should occur whenever the fluid shear stress σ_f and the capillary stress σ_c are of the same magnitude (See Figure 2.). But, for the cases where the necrotic core is more viscous ($\beta = 0.01, 0.1, 1$), the proliferative rim is not able to deform the necrotic core and hence instabilities are not formed. However, the onset of mechanical instabilities of high wave-number can be seen for the cases of $\beta = 1, Ca = 0.01$ and $\beta = 1, Ca = 0.1$.

Although the cases corresponding to $\beta = 10$ portray dramatic transformations from the initial spherical shape, they do not represent invasion in the property variations that apply to a real MCTS ($\beta < 1, Ca < 0.1$). The cases $\beta < 1$ imply that the necrotic core is more viscous than the proliferative rim which is expected in a Multi-Cellular Tumor Spheroid. Instead, these shapes are representative of the development of alveolar tissues in lungs as they can be regarded as a thick membrane evolving with a thinner fluid inside. Here, this is because proliferative cells are more motile and have a smaller associated time constant and thereby a much smaller viscosity. Hence, additional effects need to be explored to develop a more accurate representation of tumor growth and invasion. Some of these include the traction forces exerted by the tumor on its micro-environment and the release of Matrix-Metallo-Proteinases (MMPs) to facilitate invasion in addition to mechanical instabilities.

The profile for the magnitude of the velocity after 12-time constants is shown in figure 2.5. The cases with the growing finger-like morphologies have a high velocity at the tips. This might be because as the spheroid buckled, the outward-facing region experi-

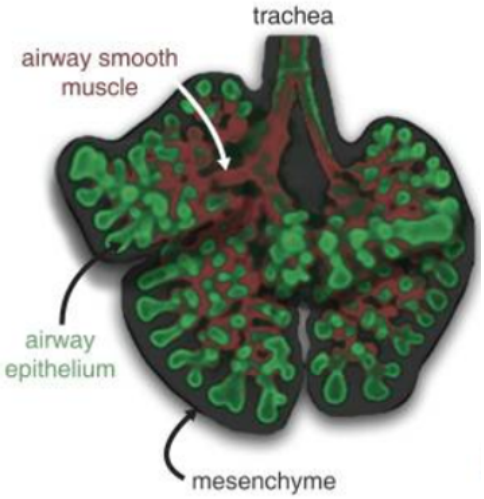

Figure 2.11: A diagram showing the airway epithelial conduits that form during lung develpment [65]

enced a sudden jump in velocity and the inner fluid (regions farther away than 1λ) got pushed into the tips, further accentuating the finger-like morphologies. Also, although the spheroids for cases $(\beta = 0.01, Ca = 10)$ through $(\beta = 1, Ca = 10)$ do not appear to have any flow in the necrotic core, there is a small backflow towards the center of the spheroid as shown in figure 2.8. This is because the cell division inside the proliferative rim occurs in all directions pushes and against the necrotic core and introduces a backflow.

As per the plots on the normalized shear rates, in all parameter sets, the region of lower viscosity has a higher shear rate which is why the proliferative rim has a high shear rate for $\beta < 1$ and the necrotic core has a larger shear rate for $\beta = 10$. An interesting observation is the presence of low shear rate regions only at the junctions of the $\beta = 10$ parameter cases.

Finally, in the normalized pressure profiles, the cases of $\beta = 10$, experience a negative pressure in their necrotic cores as the proliferation rim deposits low viscosity necrotic core

material and pulls it from the invasive front leaving a low-pressure zone in the center. Similarly, all the cases from ($\beta = 0.01, Ca = 0.01$) through ($\beta = 1, Ca = 1$), also have negative pressures in their necrotic cores, but the magnitudes of these pressures are much smaller than the $\beta = 10$ case. This is because the necrotic core is more viscous in the lower β cases and fluid motion is slower. The cases of $Ca = 10$ for the lower β cases do not have negative pressure throughout the simulation, because the higher surface tension compresses the proliferative rim and the necrotic core giving a positive pressure.

2.11 Conclusions

Although the incompressible Newtonian fluid model of the Spheroid implementing the Stokes law condition offers much insight into the mechanical fields characteristic of different types of cell aggregates, it does not predict any mechanical instabilities in the physiologically correct parameter regimes ($\beta = 0.01, Ca = 0.01$ to $\beta = 0.1, Ca = 0.1$). This implies that the mechanics of the tumor spheroid alone during its growth and with the presence of solid-to-fluid phase transition is not sufficient to predict mechanical instabilities that can facilitate invasion. Hence, a more accurate model which implements the effects of active forces experienced by the spheroid has been explored in the next chapter.

Chapter 3

Two-phase model of Tumor spheroids applying Active Stresses

3.1 Introduction

The previous demonstrate that proliferation alone cannot describe an invasive phenotype in an MCTS. However, some important mechanobiological features of cancer cells are not included in this model. For instance, cancer cells are known to apply traction forces, using various structures such as lamellopodia and filopodia on their micro-environment that helps them leave the primary tumor site. The model described in this chapter aims to simulate tumor growth after an MCTS has fluidized its micro-environment and applies active forces on an unfluidized matrix at an arbitrary distance of fluidized region. This distance is assumed to be large in this model and that the presence of the unfluidized matrix does not affect tumor invasion.

The chapter begins with a description of the 2D geometry considered, the governing differential equations solved for, the results that describe the formation of two types of

instabilities - one caused due to proliferation alone and another due to the application of active stresses.

3.2 Computational Domains

This model was solved in the planar 2D geometry. Figure 3.1 shows the computational domain and the relevant boundary conditions applied.

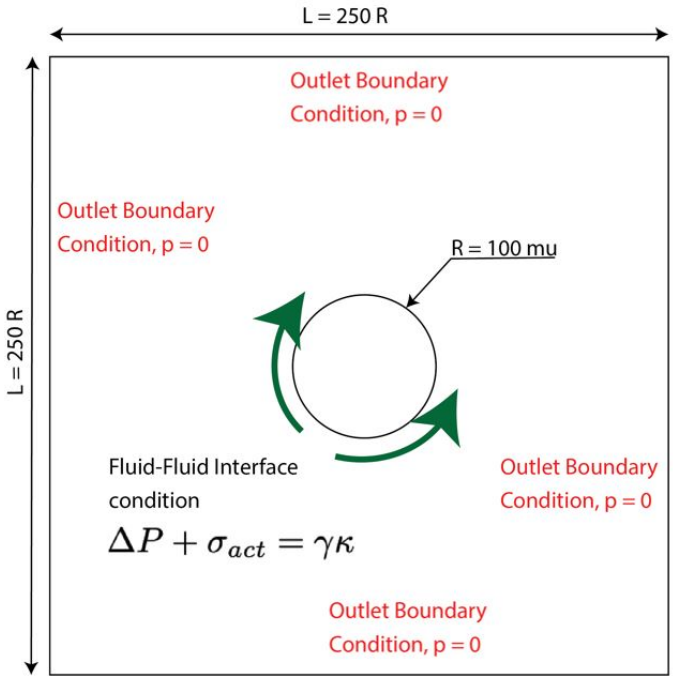

Figure 3.1: The geometry of the 2D planar computational model for spheroid growth with active stresses

3.3 Governing Differential Equations

The governing differential equations for these models are the same as in the previous section, with the addition of the equations describing active stresses on the spheroid-micro-environment boundary condition (along with surface tension) and the profile of

viscosity in the micro-environment as a consequence of ECM remodeling. In domain I, the steady-state incompressible continuity equation with the source term and the Navier-Stokes equations are solved along with the Arbitrary Lagrangian-Eulerian Algorithm as described in the previous chapter;

$$\rho \boldsymbol{\nabla} \cdot \boldsymbol{u_1} = G(r, z) \tag{3.1}$$

$$-\boldsymbol{\nabla} \cdot p_1 \boldsymbol{I} + \mu_1(r, z) \boldsymbol{\nabla} \cdot \left[\boldsymbol{\nabla} \boldsymbol{u_1} + (\boldsymbol{\nabla} \boldsymbol{u_1})^T - \frac{2}{3} \boldsymbol{\nabla} \cdot \boldsymbol{u_1} \right] = 0 \tag{3.2}$$

Where $G(r, z)$ and $\mu(r, z)$ are the same functions defined in section (2.6.2). In domain II, the continuity equations and the conservation of momentum equations are solved;

$$\rho \boldsymbol{\nabla} \cdot \boldsymbol{u_2} = 0 \tag{3.3}$$

$$-\boldsymbol{\nabla} \cdot p_2 \boldsymbol{I} + \mu_2(r, z) \boldsymbol{\nabla} \cdot \left[\boldsymbol{\nabla} \boldsymbol{u_2} + (\boldsymbol{\nabla} \boldsymbol{u_2})^T \right] = 0 \tag{3.4}$$

These governing equations are again subject to the boundary conditions;

$$n_j(\sigma_{ij}^{(1)} - \sigma_{ij}^{(2)}) = \gamma(\boldsymbol{\nabla} \cdot \hat{\boldsymbol{n}}) n_i \tag{3.5}$$

where;

$$\sigma_{ij} = -p\delta_{ij} + \mu(\boldsymbol{x}, \lambda)\dot{\epsilon}_{ij}$$

$$p_2 = 0 \tag{3.6}$$

which represents the outlet conditions on all four sides. Equations (3.1) through (3.6) represent the governing differential equations solved for this system.

3.4 Active Surface Stresses

These equations are subject to the boundary conditions shown in figure 3.1. The most important change is the implementation of the spheroid-micro-environment interface boundary condition. The spheroid exerts an active force on the surroundings and the resulting reaction from the force causes the spheroid to propel itself out of the 3D spheroid. Here, this propelling force has been introduced via the boundary condition. The applied active stresses have been included as a normal inside the tumor spheroid and it can be interpreted as a change in the local co-efficient of surface tension.

There are scarce studies that describe the system variables on which the effective co-efficient could depend. While there could be multiple ways to model this active stress, an interesting paper recently published [66] demonstrated that tumor invasion progresses in multiple invasive fronts that are initiated from regions of high curvature. As the amount of active stresses experienced by the invading cells is larger, it can be deduced that the amount of active force sustained by these cells increases with the local curvature of the spheroid surface. Hence, the active stress is varied as a function of the local mean curvature.

In this study, the stresses resulting from the traction forces are modeled as increasing

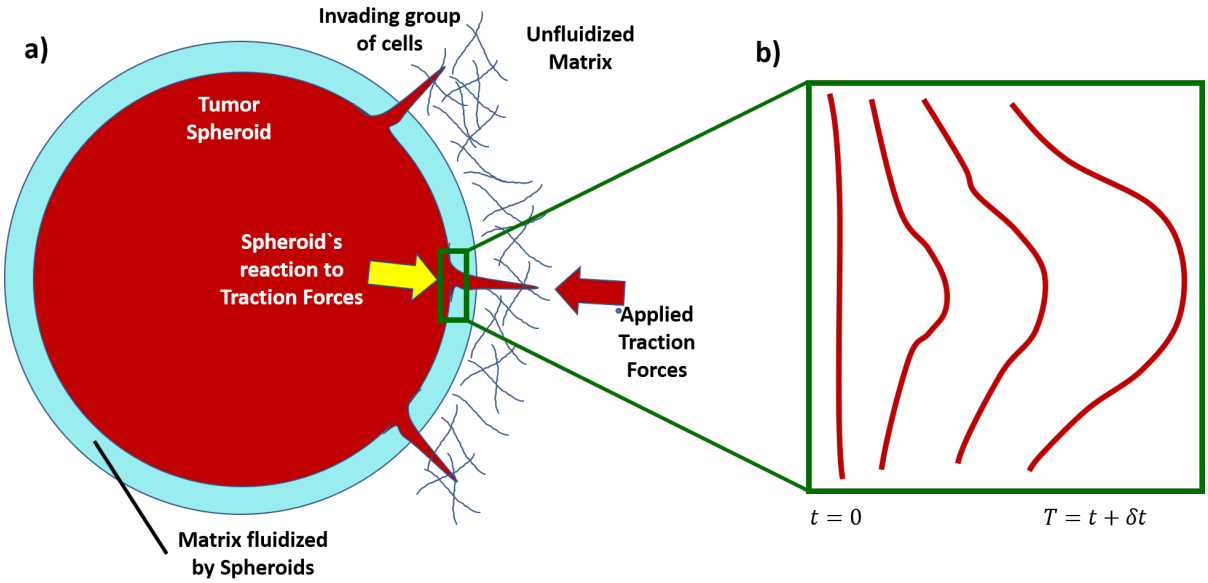

Figure 3.2: a) A simplified image of cells invading, the traction forces the invading front applies and the reaction to the traction forces. The invading cells apply forces on the surrounding matrix and the reaction results in an increase in stress in the normal direction which is transmitted to the bulk of the spheroid. b) By making the magnitude of active stresses curvature dependent, it is possible to model cancer invasion, initiated by perturbations in local mean curvature.

with the square of the curvature and no forces are experienced when the curvature is positive. Thus, regions of higher surface tension will experience a larger normal stress in the direction of the normal (see figure 3.3).

$$\sigma_A = \zeta H^2$$

Numerical perturbations introduced by COMSOL's descritization will cause some regions to experience a higher stress than others. These perturbations will grow in size as the active stress increases with the local mean curvature and eventually introduce instabilities

in the system. Hence, σ_A is re-written as;

$$\sigma_A = \begin{cases} 0 & H \geq 0 \\ \zeta H^2 & H < 0 \end{cases} \tag{3.7}$$

Where ζ is a constant with units of force - N, where H is the curvature defined as $H = -\boldsymbol{\nabla} \cdot \hat{\boldsymbol{n}}$, where $\hat{n}$ is the unit outward normal. Defining the stress states of each domain as;

$$\sigma_{ij} = -p\delta_{ij} + \mu(\boldsymbol{x}, \lambda)\tilde{\dot{\epsilon}}_{ij}$$

Where p is the pressure, δ_{ij} is the Kronecker delta, μ is the viscosity function and is dependent on the position of the moving interface $\boldsymbol{x}$ and the thickness of the proliferative rim λ. $\tilde{\dot{\epsilon}}_{ij}$ is the strain rate tensor at the interface between the spheroid and the micro-environment domain, the boundary condition that relates the discontinuity between the stress states of domain 1 and domain 2 is solved. This is obtained from a balance of forces;

$$n_j(\sigma_{ij}^{(1)} - \sigma_{ij}^{(2)}) = \gamma(\nabla \cdot \hat{\boldsymbol{n}})n_i$$

When the cells apply forces, the state of stress in domain 1 changes to;

$$\sigma_{ij,inv}^{(1)} = -(p + \sigma_A)\delta_{ij} + \mu(\boldsymbol{x}, \lambda)\tilde{\dot{\epsilon}}_{ij}$$

$$\implies \sigma_{ij,inv}^{(1)} = \sigma_{ij}^{(1)} - \sigma_A\delta_{ij}$$

Hence, Equation (3.5) can be re-written as;

$$n_j(\sigma_{ij}^{(1)} - \sigma_A - \sigma_{ij}^{(2)}) = \gamma(\boldsymbol{\nabla} \cdot \hat{\boldsymbol{n}})n_i$$

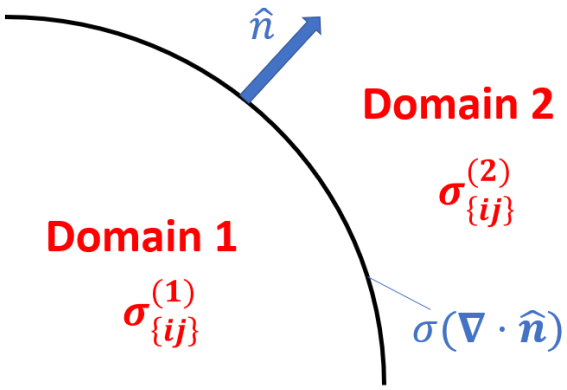

Figure 3.3: A diagram explaining the definitions of domains (1) and (2) and the direction of the outward normal and the capillary stress in the boundary.

Expressing as defined in equation (3.6);

$$\implies n_j(\sigma_{ij}^{(1)} - \sigma_{ij}^{(2)}) = \gamma(\boldsymbol{\nabla} \cdot \hat{\boldsymbol{n}})n_i + \zeta(\boldsymbol{\nabla} \cdot \hat{\boldsymbol{n}})^2 n_i$$

$$\implies n_j(\sigma_{ij}^{(1)} - \sigma_{ij}^{(2)}) = [\gamma + \zeta(\boldsymbol{\nabla} \cdot \hat{\boldsymbol{n}})](\boldsymbol{\nabla} \cdot \hat{\boldsymbol{n}})n_i \tag{3.8}$$

Hence, the afore-mentioned effective co-efficient of surface tension is given as;

$$\gamma_{eff} = [\gamma + \zeta(\boldsymbol{\nabla} \cdot \hat{\boldsymbol{n}})] \tag{3.9}$$

COMSOL automatically calculates the local curvature of the boundaries in a variable called *curv_spatial*. Which is defined as;

$$curv\_spatial = -\boldsymbol{\nabla} \cdot \hat{\boldsymbol{n}}$$

Where $\hat{n}$ is the unit outward normal. To use this variable effectively, two functions are

defined in COMSOL - *smooth_curv*11, a moving average filter that interfaces between MATLAB and COMSOL and the force function that changes the sign for use in effective surface tension coefficient as described by equation (3.6). The function *smooth_curv*11 is gaussian averaged moving average filter implemented by using the built-in MATLAB function smooth data(). During the execution, COMSOL calls the MATLAB function and sends it a vector containing the variable *curv_spatial* from each mesh node. MATLAB applies the gaussian-weighted moving average filter and returns the data to COMSOL, which is then processed by the $force()$ function;

$$force(H) = \begin{cases} 0 & H \geq 0 \\ -H & H < 0 \end{cases} \tag{3.10}$$

*smooth_curv*11 was able to smooth significant curvature variations. For instance, at time =0, the two vertices present in the initial spheroid surface introduced a large discontinuity (almost 50% of mean curvature value). The smoothing function was able to reduce to less this discontinuity to less than 3% variation. However, COMSOL also introduced small numerical errors in the smoothed data. The corresponding data, when analyzed in MATLAB, did not present these variations. Hence, it is potentially caused by some round-off error introduced by COMSOL.

The remaining boundary conditions of the micro-environment are four outlets at zero pressure boundary condition $\tilde{p}$. The axial symmetry boundary condition does not apply in this case as this is a full 2D model. This is an important change as the presence of the axial symmetry condition could introduce numerical instabilities after the spheroid has buckled.

3.5 Scaling of Equations

As described in the previous chapter, the characteristic length and time scales in the system are defined as $\tau = 108,000s$, the cell division time and $\lambda = 50\mu m$ the length of the proliferative rim of the spheroid. Using these constants, we can non-dimensionalize equations (3.1)-(3.6).

$$\tilde{t} = \frac{t}{\tau}, \tilde{\boldsymbol{x}} = \frac{\boldsymbol{x}}{\lambda}, \tilde{\boldsymbol{U}} = \frac{\boldsymbol{U}\tau}{\lambda}$$

$$\rho\frac{\tilde{\boldsymbol{\nabla}}}{\lambda} \cdot \frac{\tilde{\boldsymbol{u}}_{\mathbf{1}}\lambda}{\tau} = G(r,z)$$

Equation 3.1 becomes;

$$\tilde{\boldsymbol{\nabla}} \cdot \tilde{\boldsymbol{u}}_{\mathbf{1}} = \frac{\tau}{\rho}G(r,z) \tag{3.11}$$

As explained in section (2.6.2), the cell division rate G is held constant and the parameter;

$$\frac{G\tau}{\rho} = \Omega$$

is defined as the Cell division control parameter. Similarly, for equation 3.2;

$$-\frac{\tilde{\boldsymbol{\nabla}} \cdot \tilde{p}_1\boldsymbol{I}}{\lambda}\sigma_s + \frac{\mu_1(r,z)}{\tau\lambda}\tilde{\boldsymbol{\nabla}} \cdot \left[\tilde{\boldsymbol{\nabla}}\tilde{\boldsymbol{u}}_{\mathbf{1}} + (\tilde{\boldsymbol{\nabla}}\tilde{\boldsymbol{u}}_{\mathbf{1}})^T - \frac{2}{3}\tilde{\boldsymbol{\nabla}} \cdot \tilde{\boldsymbol{u}}_{\mathbf{1}}\right] = 0$$

As $\mu(r,z)$ is a piece-wise function spatially defining the viscosity in the proliferative rim and the necrotic core, two stress values are arising out of this function. As before, the shear stress scale in the necrotic region is chosen to normalize the system.

$$-\tilde{\boldsymbol{\nabla}} \cdot \tilde{p}_1\boldsymbol{I} + \frac{\mu_1(r,z)}{\tau\sigma_s}\tilde{\boldsymbol{\nabla}} \cdot \left[\tilde{\boldsymbol{\nabla}}\tilde{\boldsymbol{u}}_{\mathbf{1}} + (\tilde{\boldsymbol{\nabla}}\tilde{\boldsymbol{u}}_{\mathbf{1}})^T - \frac{2}{3}\tilde{\boldsymbol{\nabla}} \cdot \tilde{\boldsymbol{u}}_{\mathbf{1}}\right] = 0$$

$$-\tilde{\boldsymbol{\nabla}} \cdot \tilde{p}_1 \boldsymbol{I} + \tilde{\mu_1}(r,z)\tilde{\boldsymbol{\nabla}} \cdot \left[\tilde{\boldsymbol{\nabla}}\tilde{\boldsymbol{u}}_{\mathbf{1}} + (\tilde{\boldsymbol{\nabla}}\tilde{\boldsymbol{u}}_{\mathbf{1}})^T - \frac{2}{3}\tilde{\boldsymbol{\nabla}} \cdot \tilde{\boldsymbol{u}}_{\mathbf{1}}\right] = 0 \tag{3.12}$$

Where

$$\tilde{\mu}(r,z) = \begin{cases} \frac{\mu_r}{\mu_s} = \beta & d_R(\tilde{r},\tilde{z}) \leq 1 \\ \\ \frac{\mu_s}{\mu_s} = 1 & d_R(\tilde{r},\tilde{z}) > 1 \end{cases}$$

$$\tilde{\boldsymbol{\nabla}} \cdot \tilde{\boldsymbol{u}}_{\mathbf{2}} = 0 \tag{3.13}$$

The equation 3.4 for the governing differential equations inside the non-newtonian micro-environment, the shear stress in the necrotic core is used to scale the pressure and active stresses;

$$-\tilde{\boldsymbol{\nabla}} \cdot \tilde{p}_2 \boldsymbol{I} + \frac{\mu_2(r,z)}{\tau\sigma_s}\tilde{\boldsymbol{\nabla}} \cdot \left[\tilde{\boldsymbol{\nabla}}\tilde{\boldsymbol{u}}_{\mathbf{2}} + (\tilde{\boldsymbol{\nabla}}\tilde{\boldsymbol{u}}_{\mathbf{2}})^T\right] = 0$$

Where κ is the ratio of the medium shear stress to the shear stress in the necrotic core.

$$-\tilde{\boldsymbol{\nabla}} \cdot \tilde{p}_2 \boldsymbol{I} + \kappa\tilde{\boldsymbol{\nabla}} \cdot \left[\tilde{\boldsymbol{\nabla}}\tilde{\boldsymbol{u}}_2 + (\tilde{\boldsymbol{\nabla}}\tilde{\boldsymbol{u}}_2)^T\right] = 0 \tag{3.14}$$

3.5.1 Normalizing the Interfacial Tension Boundary Condition

Equation (3.9) is normalized using the shear stress in the necrotic core and normalizing the gradient operators using the characteristic length scale λ

$$n_j\left(\tilde{\sigma}_{ij}^{(1)} - \tilde{\sigma}_{ij}^{(2)}\right)\sigma_s = \frac{1}{\lambda}\gamma\left(\tilde{\boldsymbol{\nabla}} \cdot \hat{\boldsymbol{n}}\right)n_i$$

$$n_j(\tilde{\sigma}_{ij}^{(1)} - \tilde{\sigma}_{ij}^{(2)}) = Ca(\tilde{\boldsymbol{\nabla}} \cdot \hat{\boldsymbol{n}})n_i \tag{3.15}$$

Where Ca is the Capillary number and is defined as the ratio of the capillary stress to the shear stress in the necrotic core;

$$Ca = \frac{\sigma_c}{\sigma_s} = \frac{\gamma\tau}{\lambda\mu_s}$$

which can also be interpreted as the ratio of the proliferation rim thickness λ and an intrinsic length scale defined as;

$$l = \frac{\tau\gamma}{\mu_s}$$

Constant pressure outlet boundary condition;

$$\tilde{p}_2 = 0 \tag{3.16}$$

Equations (3.11) through (3.16) represents the fully scaled governing differential equations and boundary conditions for the model exploring growth-induced instabilities.

3.5.2 Non-dimensionalized equations for Active Surface Stress Simulations

The model exploring the instabilities due to the active stress is different from the model in the previous section. In this model, growth is neglected and hence a characteristic time scale associated with proliferation is does not exist in the system. A different time-scale needs to be defined. The length scale of the viscosities λ is still used here.

As defined previously, the active stress is considered to be proportional to the square of the local mean curvature (Equation 3.7). The stress-scale that arises out of this formula is given by;

$$\sigma_A^0 = \frac{\zeta}{\lambda^2}$$

Using this, a time-scale can be defined;

$$\tau_A = \frac{\mu_r}{\sigma_A^0}$$

These stress, length and time-scales can be used to nondimensionalize the Stokes flow equation as before. In domain 1;

$$\tilde{\boldsymbol{\nabla}} \cdot \tilde{\boldsymbol{u}}_{\mathbf{1}} = 0 \tag{3.17}$$

$$-\frac{\tilde{\boldsymbol{\nabla}}}{\lambda} \cdot \tilde{p}_1 \boldsymbol{I} \sigma_A^0 + \mu(r,z) \frac{\tilde{\boldsymbol{\nabla}}}{\lambda} \cdot \left[\frac{\tilde{\boldsymbol{\nabla}}}{\lambda} \tilde{\boldsymbol{u}}_{\mathbf{1}} \frac{\lambda}{\tau_A} + \left(\frac{\boldsymbol{\nabla}}{\lambda} \tilde{\boldsymbol{u}}_{\mathbf{1}} \frac{\lambda}{\tau_A} \right)^T \right] = 0$$

$$\implies -\tilde{\boldsymbol{\nabla}} \cdot \tilde{p}_1 \boldsymbol{I} + \mu(r,z) \frac{\tilde{\boldsymbol{\nabla}}}{\tau_A \sigma_A^0} \cdot \left[\tilde{\boldsymbol{\nabla}} \tilde{\boldsymbol{u}}_{\mathbf{1}} + \left(\boldsymbol{\nabla} \tilde{\boldsymbol{u}}_{\mathbf{1}} \right)^T \right] = 0$$

$$\implies -\tilde{\boldsymbol{\nabla}} \cdot \tilde{p}_1 \boldsymbol{I} + \tilde{\mu}(r,z) \tilde{\boldsymbol{\nabla}} \cdot \left[\tilde{\boldsymbol{\nabla}} \tilde{\boldsymbol{u}}_{\mathbf{1}} + \left(\boldsymbol{\nabla} \tilde{\boldsymbol{u}}_{\mathbf{1}} \right)^T \right] = 0 \tag{3.18}$$

Where

$$\tilde{\mu}(r,z) = \begin{cases} \frac{\mu_r}{\mu_r} = 1 & d_R(\tilde{r},\tilde{z}) \leq 1 \\ \frac{\mu_s}{\mu_r} = \frac{1}{\beta} & d_R(\tilde{r},\tilde{z}) > 1 \end{cases}$$

The equations for domain II can be scaled in the similar way. Next, the interfacial tension incorporating the curvature dependent boundary condition is scaled. Using Equation (3.8);

$$n_j(\tilde{\sigma}_{ij}^{(1)} - \tilde{\sigma}_{ij}^{(2)})\sigma_A^0 = \left[\gamma + \zeta\left(\frac{\tilde{\boldsymbol{\nabla}}}{\lambda} \cdot \hat{\boldsymbol{n}}\right)\right](\frac{\tilde{\boldsymbol{\nabla}}}{\lambda} \cdot \hat{\boldsymbol{n}})n_i$$

$$\implies n_j(\tilde{\sigma}_{ij}^{(1)} - \tilde{\sigma}_{ij}^{(2)}) = \left[\frac{\gamma\lambda^2}{\zeta} + \zeta\left(\frac{\tilde{\boldsymbol{\nabla}}}{\sigma_A^0\lambda} \cdot \hat{\boldsymbol{n}}\right)\right](\frac{\tilde{\boldsymbol{\nabla}}}{\lambda} \cdot \hat{\boldsymbol{n}})n_i$$

$$\implies n_j(\tilde{\sigma}_{ij}^{(1)} - \tilde{\sigma}_{ij}^{(2)}) = \left[\frac{\gamma\lambda}{\zeta} + \tilde{\boldsymbol{\nabla}} \cdot \hat{n}\right](\tilde{\boldsymbol{\nabla}} \cdot \hat{\boldsymbol{n}})n_i$$

$$\implies n_j(\tilde{\sigma}_{ij}^{(1)} - \tilde{\sigma}_{ij}^{(2)}) = \left[\frac{1}{\alpha} + \tilde{\boldsymbol{\nabla}} \cdot \hat{n}\right](\tilde{\boldsymbol{\nabla}} \cdot \hat{\boldsymbol{n}})n_i \tag{3.19}$$

Where $\alpha = \frac{\zeta}{\lambda\gamma}$. Hence, it can be interpreted that large values of α results in the first term diminishing and the non-dimensional curvature term begins to dominate, resulting in instabilities that depend on the curvature.

3.6 Computational Results

3.6.1 Validation of 2D Axisymmetric model in Planar model

As is required after any radical change made to the dimensionality of a theoretical model, the first step taken here is validating the results of the previous model in a 2-dimensional domain. Here, the spheroid and the micro-environment are planar models.

The case specifically for $Ca = 0.01$ is studied as it contains interesting transitions as β varies from 0.01 to 10. From figure 3.2, it is evident that physical phenomena observed such as buckling is conserved for both types of geometry - 2D axisymmetric and planar 2D

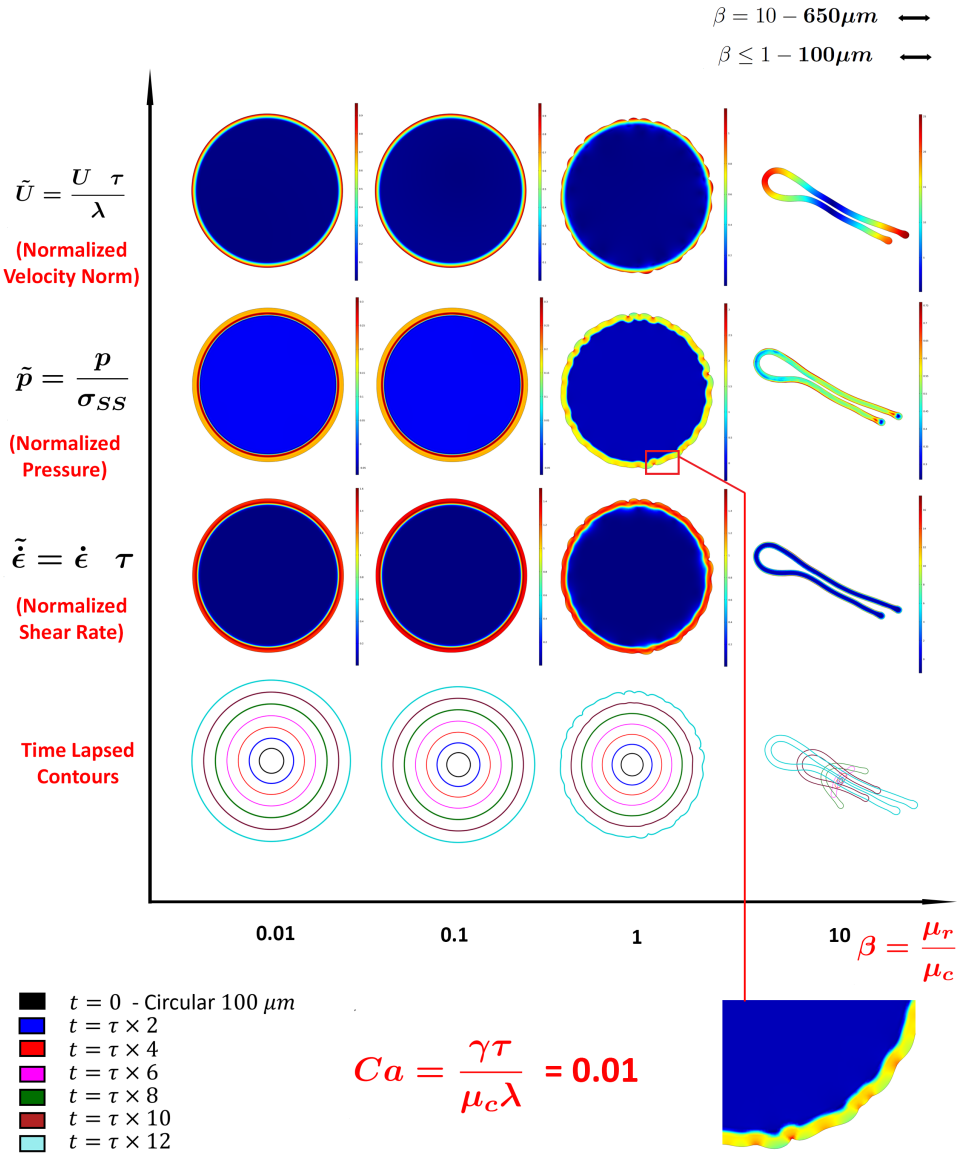

Figure 3.4: Revalidation model results of spheroid contours, normalized velocity, shear rates and pressures for a parametric sweep for Capillary number (0.01) $\frac{\sigma_c}{\sigma_s}$ and ratio of viscosities (0.01-10) $\frac{\mu_r}{\mu_s}$ for 12 time constants (τ)

cases and is independent of the axial symmetry boundary condition imposed by comsol in the previous chapter.

3.6.2 Computational Results for Spheroids exhibiting Growth Induced Instabilities

The model described in the previous sections was simulated without any active stresses, i.e., by setting $\alpha = 0$. This was done to examine potential growth induced instabilities. From the model in the previous chapter, it was shown that for the fixed proliferation rim length of λ, the physiologically relevant regime ($Ca = 0.01, \beta = 0.1$) did not produce any instabilities. Here, the dimensionless parameter $\frac{\lambda}{l}$ is varied over different values and instabilities similar to creasing instabilities are observed for the parameters $\beta = 0.1$ and $Ca = 0.01$, with a instabilities occurring between, but not including, $\frac{\lambda}{l} = 0.25, 0.5$ and $\frac{\lambda}{l} = 100$.

3.6.3 Computational Results for Spheroids exhibiting Normal Curvature Dependent Active Stresses

The parametric sweep is calculated between β, the ratio of core to rim viscosities and α, the ratio of the active stress to the capillary stress. The parameters examined are $\alpha = 150, 250, 500, 1000$ and $\beta = 10^{-4}, 10^{-3}, 0.01, 0.1$. Also, as the simulations were computationally expensive, they were simulated only until 0.1τ in some cases. However, the instability that can cause invasion is already evident in these cases and the calculation becomes more difficult due to the highly non-linear shape of the spheroid before the invasion. As the active stresses are imposed on the system after the spheroid assumes a large curvature, the imbalance in the momentum equation causes the spheroid to drift. This was considered as the stopping point for these simulations. The results of these simulations are shown below.

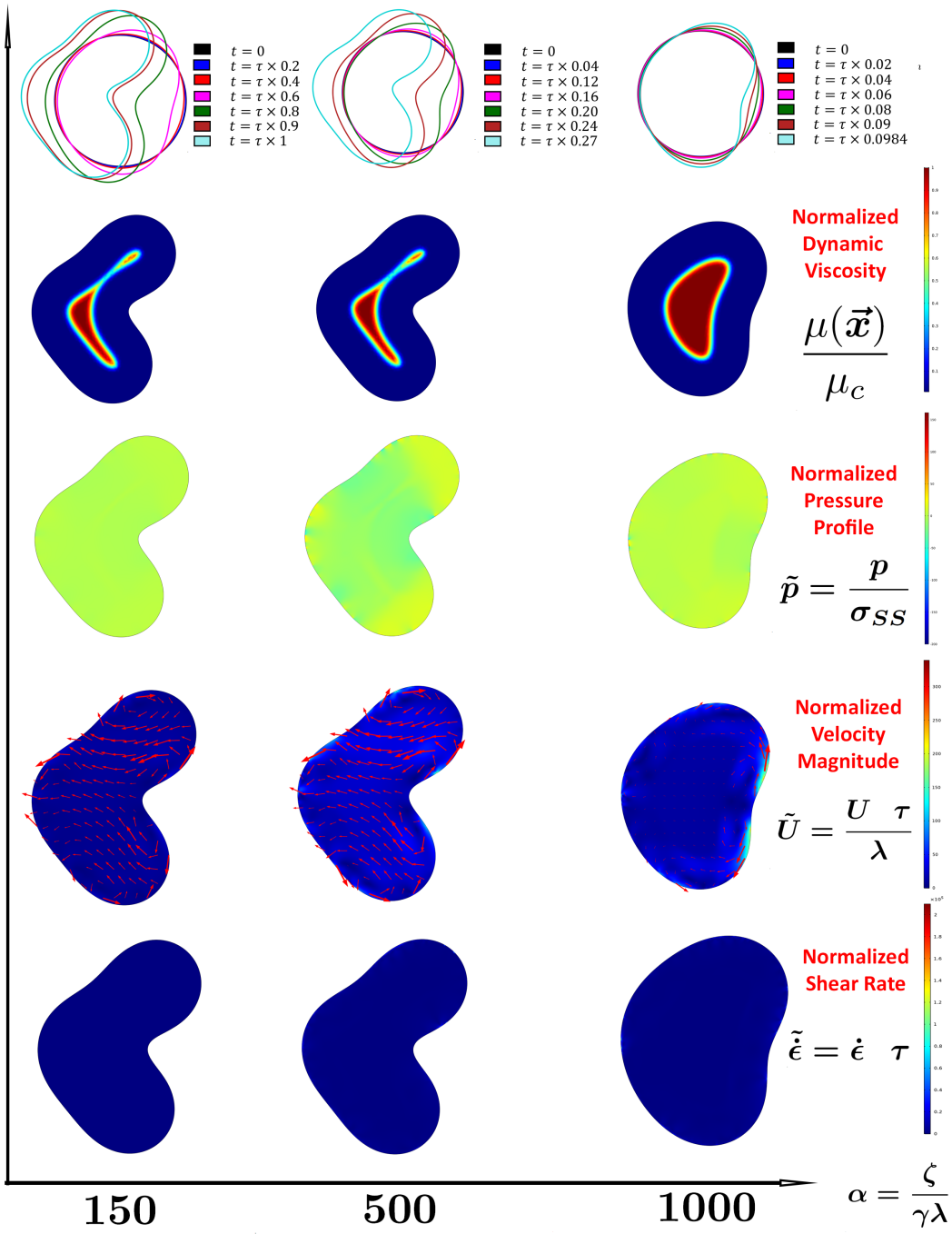

Figure 3.5: Simulation Results for Spheroid growth and field variables for $\beta = \frac{\mu_r}{\mu_s} = 0.01$, $Ca = \frac{\sigma_c}{\sigma_s} = 0.01$ for 3 different values of $\alpha = 150, 500, 1000$

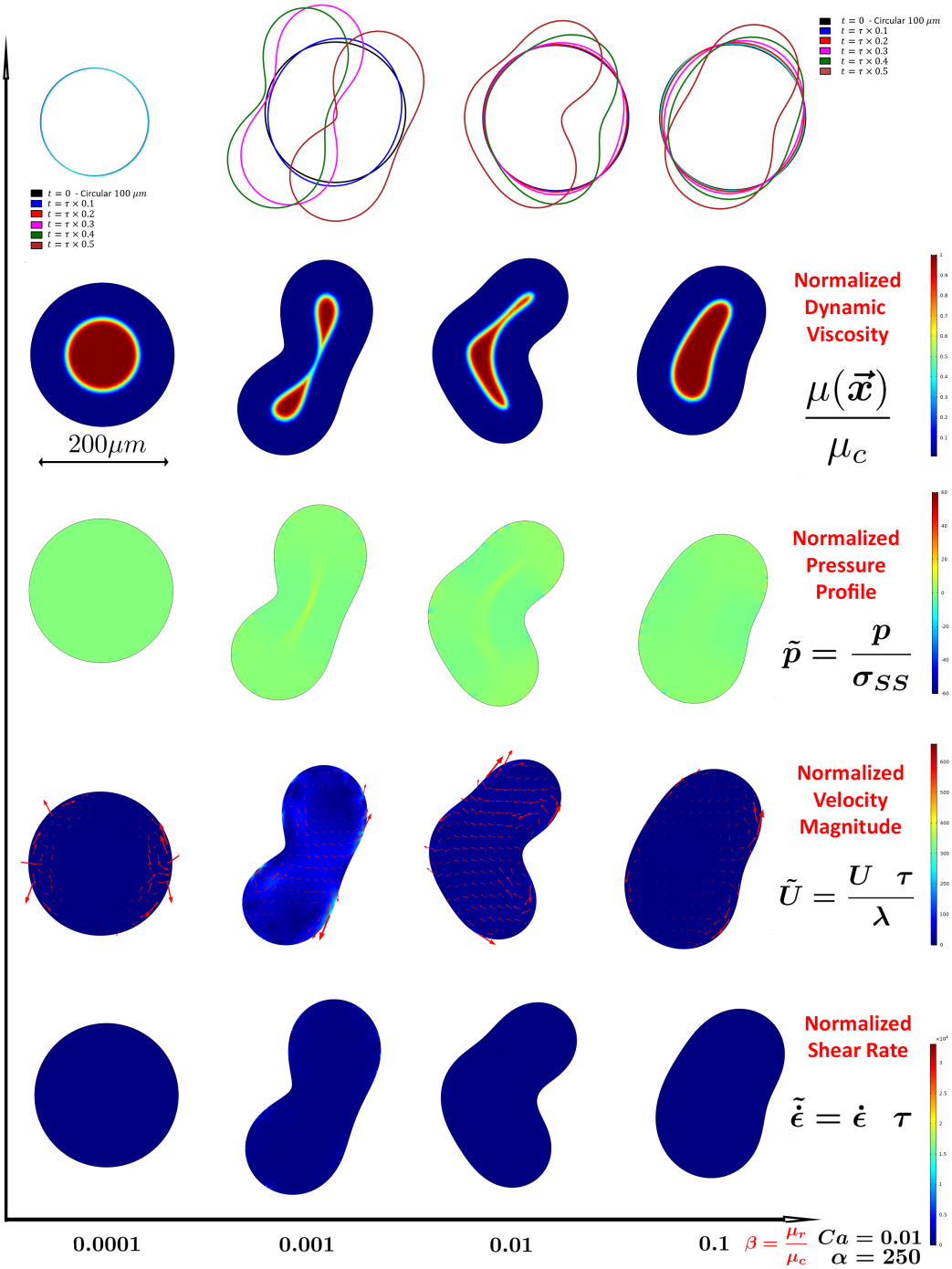

Figure 3.6: Simulation Results for Spheroid growth and field variables for $\alpha = \frac{\zeta}{\gamma\lambda} = 250$, $Ca = \frac{\sigma_c}{\sigma_s} = 0.01$ for 4 different values of $\beta = 0.0001, 0.001, 0.01, 0.1$

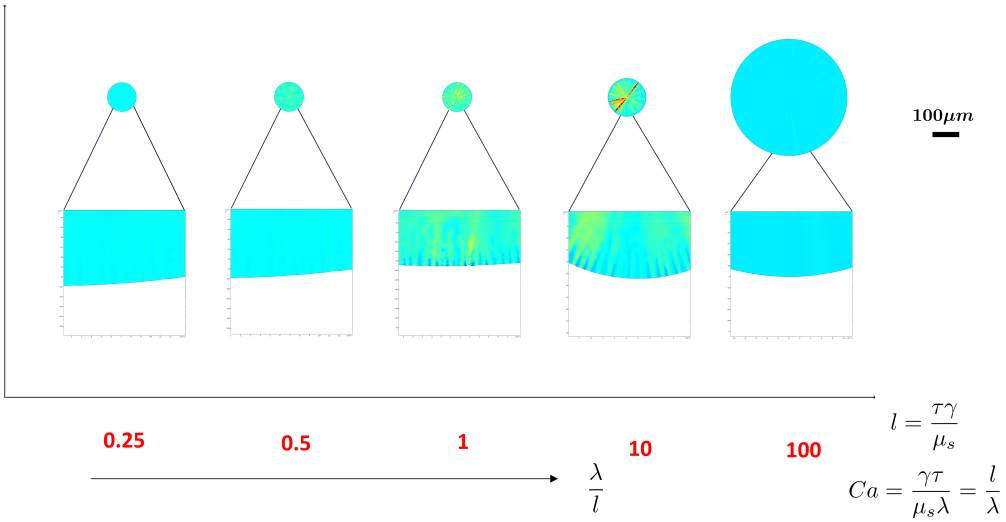

Figure 3.7: Instabilities originating due to spheroid growth by varying the thickness of the proliferating rim by varying the dimensionless parameter $\frac{\lambda}{l}$

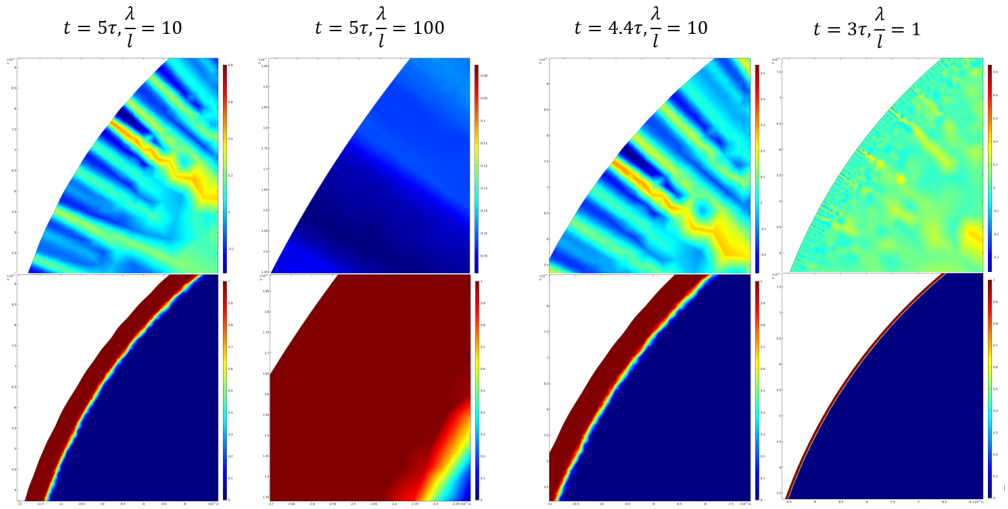

Figure 3.8: The rate at which the instabilities form on the spheroid surface depends on the length of the proliferation rim. Left - For the same amount of time, the curvature variations are obtained faster for $\frac{\lambda}{l} = 10$ and similarly, changes in curvature are faster for $\frac{\lambda}{l} = 1$

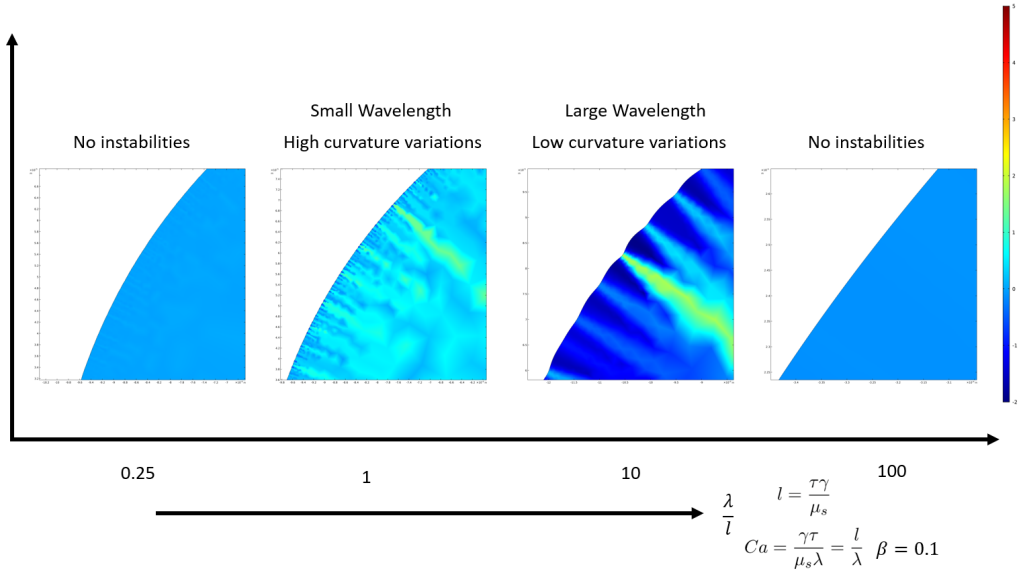

Figure 3.9: Instabilities originate when the dimensionless parameter $\frac{\lambda}{l}$ is within a specific range.

3.7 Discussion

This chapter first investigates the instabilities due to cell division. Here, the relevance of the thickness of the proliferative rim is examined. According to figure (3.7), we find that the growth-induced instabilities seem to depend on the length of the proliferative rim. The three variables of interest here are the time scale of these instabilities, the extent of the variation in curvature and the wavelengths formed. According to figure (3.7) and (3.9), the cases corresponding to the extreme cases of the proliferation-zone thickness values do not form any instabilities. This is because in the case $\frac{\lambda}{l} = 0.25$, the rim is so small relative to the MCTS that, the accumulation of mass is at a small rate. Due to this, the instabilities will take a significant amount of time to form. In the case for $\frac{\lambda}{l} = 100$, the large rate of proliferation smooths out the formation of instabilities and hence will take a large amount of time for instabilities to form.

But, in the cases $\frac{\lambda}{l} = 1$ and $\frac{\lambda}{l} = 10$, instabilities are visible. Here, a low proliferation-

zone thickness results in instabilities of high variations in curvature and correspondingly small wavelengths. These curvature variations diminish as the length of the proliferation zone increases and finally disappears within in the examined time-scale. This physically means that if the MCTS wishes to introduce an increasingly wavy profile on its surface within a specific period of time, the necrotic core should have a larger radius. This is consistent because a large proliferation rim means that a large part of the MCTS is still dividing and it does not permit the outermost cells to escape from the free surface.

Next, we investigate the effect of adding curvature dependent normal-active stresses. In this formulation, the parameters varied are the ratio of rim-to-necrotic core viscosities β and the dimensionless parameter α. The sweeps done was for values of α 150, 500 and 1000 and for $\beta, 10^{-4}, 10^{-3}, 0.01$ and 0.1.

3.7.1 Varying Active Stress, keeping Viscosity Profile Same

The results calculated are shown in figure 3.3. According to the model, if the value of β is held constant, the active forces attempt to deform the spheroid to the same shape. This means that β or the differences in the viscosity inside the spheroid controls the shape of the instability, while α controls the time scale of the emergence of these instabilities. This is evident from the legends specified for the time-lapsed contours specified on the top row of the figure (3.5). From these, it is evident that the time scale of the instability almost inversely scales with the parameter α;

$$\frac{t_{M,\alpha=500}}{t_{M,\alpha=150}} = \frac{0.27}{1} = 0.27 \approx \frac{150}{500} = 0.3$$

Higher values of α were generating the instabilities so fast that, the geometry became nonlinear by 0.1τ and could not solve further.

With the curvature-dependent normal stresses in effect, the regions of high curvature are experiencing high normal stress compared to those regions of zero or positive curvature. This results in the spheroid attempting to pinch off a part of it, which is representative of tumor invasion - where a collection of cells attempt to branch out and invade to the surrounding matrix.

It is also interesting to note the arrangement of normalized velocity vectors inside the spheroids. It is possible to observe Marangoni flows that form due to the presence of the gradients in the coefficient of interfacial tension. As explained before, the regions of high negative curvature are defined to have high coefficients of interfacial tension and baseline interfacial tension for regions of positive or zero curvature. In all cases of α, it is possible to see tangential velocity vectors starting from positive curvature regions, directed towards negative curvature regions.

3.7.2 Changing viscosity profile, keeping active stress Constant

Keeping α fixed at 250, the resulting instabilities are shown in figure (3.6). There are multiple interesting cases to be explored. As mentioned previously, the parameter appeared to control the time scale of the emergence of the instabilities. Here, for the cases of $\beta = 0.001$ and $\beta = 0.01$, the instabilities emerged by 0.5τ. However, the case of $\beta = 0.1$, it takes longer for the instabilities to appear. The case for $\beta = 10^{-4}$ is not reliable in this model, because, there was a large amount of numerical error evidenced by the drifting of the spheroid from its initial position.

As in the previous section, it is possible to see Marangoni flow setting up flow cells

inside the spheroid and appears to be different for each case of β.

3.8 Conclusion

The study presented in this chapter explores two kinds of instabilities. One due to growth and another due to the application of normal active stresses. The instabilities due to growth are reminiscent of creasing instabilities and depend on the thickness of the proliferative rim. The wave-number of these instabilities also appear to be dictated by the inverse Capillary number ($\frac{1}{Ca}$ interpreted as $\frac{\lambda}{l}$).

The instabilities due to the normal active stresses demonstrate the tendency of the spheroid to pinch off, to invade its surroundings. The parameter β appears to control the shape of the instabilities formed and the parameter α appears to control the time scale of their emergence.

Unlimited growth and invasive potential are 2 among the most dangerous hallmarks of any cancer. Unlimited growth can lead to disruption of the functioning of local organs and invasion can result in the tumor attacking the host body on a global scale. It is possible that tumor cells could use both these techniques simultaneously. Hence, it is important to understand the instabilities caused by these cases individually to fully appreciate their combined effect in the future.

Chapter 4

Troubleshooting Experiments to validate theoretical models

4.1 Introduction

The conclusions from the previous chapter indicate that the inhomogeneities in aggregate mechanics, applied active stresses and growth can affect invasion. The current chapter describes a potential experimental outline to which I contributed to validate these theoretical predictions.

As mentioned briefly in the first chapter, many techniques can be used to investigate the mechanics of a biological system. However, a large majority of them are applicable only for *in-vitro* models or requires the destruction of the model to study them. Other problems include that they can only be applied to a simplified model which does not recapitulate the working of the real system. The oil droplet inserts using co-surfactant systems developed in the Campàs lab [67] is the best technique to measure the rheological properties of the system as it develops and in the case of cancer, as it proliferates and invades.

This chapter begins by explaining the oil droplet technique developed in the Campàs lab. It explains the process of inserting them into cultured MCTS and acquiring data via a confocal microscope and analyzing the results using LabVIEW. The cell lines that used and the procedures involved in developing the 2D and 3D cell cultures (spheroids) using the hanging droplet technique are explained [9], [68].

4.2 Experimental Setup

4.2.1 Oil Droplet-based magnetic micro-rheometers

As explained in [68], magnetic droplets can be used to apply magnetic stress on the surrounding tumor aggregates using a magnetic assembly. These droplets are injected into the spheroids using a pico-liter injector through glass needles. (Refer to appendix B.1 for how these oils are mixed).

4.2.2 Oil Droplet-based sensors for measuring anisotropic stresses

The anisotropic stress refers to the stress experienced by a cell in the bulk tissue due to active forces and morphogenetic flows. Measuring the trends and time scales of this stress can offer important insights into the origin of invasion related instabilities. With the oil-droplet based sensors [67] and further modified with the co-surfactant system [69], these stresses can be measured. The droplets use a co-surfactant system consisting of Krytox-PEG(600) and DSPE-biotinylated-PEG(2000) coated with Arginylglycylaspartic acid (RGD) which can ligate to the cells. These ligands can be used as adapters to transmit forces to the droplet.

The Krytox-PEG maintains the droplet interfacial tension so that γ remains constant

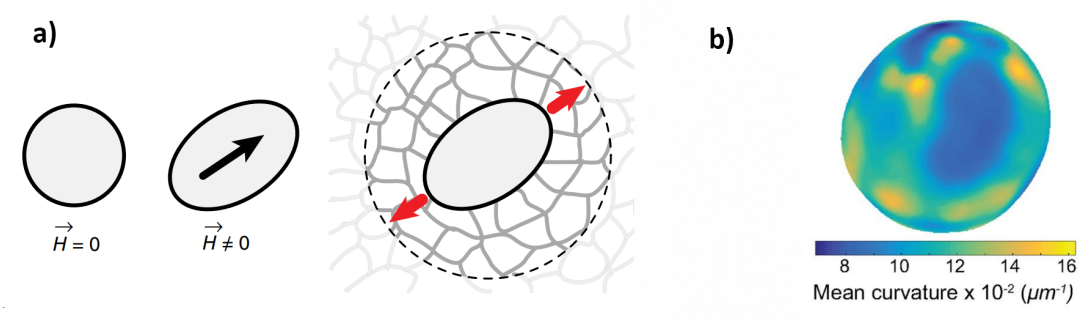

Figure 4.1: a) A schematic diagram of a magnetic droplet actuating, when the magnetic field is switched on, b) An oil droplet after recording deformations applied by surrounding cells. After post-processing, the surface heat map represents the variations in curvature which can be used to calculate the anisotropic stress components [69]

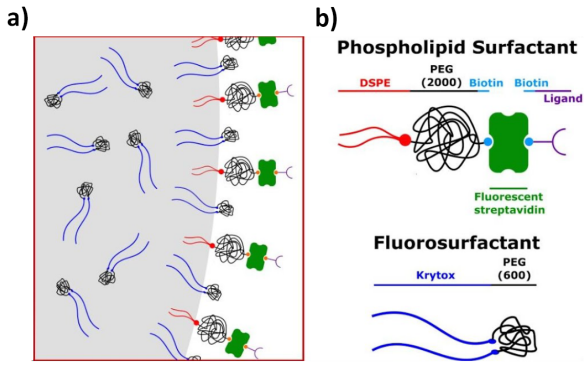

Figure 4.2: a) The co-surfactant system employed to measure the curvature variations after correctly mixing inside the oil. b) The individual surfactants employed - the DSPE-PEG(2000) biotin allows cells to ligate to the droplet and apply forces, while the Krytox-PEG(600) helps to maintain the coefficient of interfacial tension

and the DSPE-PEG-biotin allows cells to attach to the droplets and exert forces. These surfactants are also suspended in the fluorocarbon oil - Novec 7700 and due to the amphiphilic nature of the surfactants, the DSPE component remains at the surface, while the Krytox component remains inside the droplet. Writing a force equilibrium at the droplet surface;

$$\sigma_A^T = 2\gamma(H_a - H_b) \tag{4.1}$$

Where, γ is the coefficient of interfacial tension and H_a and H_b are the local curvatures at any two points on the droplet surface inside the MCTS, where σ_A^T is the local component of anisotropic stress. The distribution of these values are obtained for any two points on the droplet and the standard deviation calculated from the distribution represents the magnitude of anisotropic stress at the location of the droplet.

4.3 Data Acquisition and Processing

These non-magnetic droplets are generated using microfluidic techniques, while the magnetic droplets are injected directly from a stock of magnetic oil. Once generated and collected, they are injected into the MCTS. After injection (Appendix B.2), the MCTS is embedded inside a collagen matrix (Appendix B.3-4) and after providing sufficient time to heal the aggregates, are imaged using a Zeiss confocal microscope with an incubation chamber which maintains a temperature of 37 degrees Celcius and 5% Carbon Dioxide. Using the Confocal microscope, Time Lapsed Z-stacks of the deforming droplet are acquired and the variations in the curvature can be calculated. The curvature is calculated at the nodes on a mesh resulting from discretizing the droplet surface and reconstructing it using the z-stacks and an in-house code written in MATLAB. Equation (4.1) is applied to obtain the distribution of anisotropic stress at any two points and the standard deviation of this curve is the value of the anisotropic stress [69].

The confocal microscope housing also contains a magnetic housing with an array of 8 magnets arranged so that there is a unidirectional magnetic field at the center of the housing and no magnetic field components perpendicular to this direction. The arrangement attenuates the magnetic fields in the other two (x and y) orthogonal directions. By moving the magnets up and down - using a virtual instrument developed using LabVIEW, the applied magnetic stress can be varied. This can be used to actuate the mag-

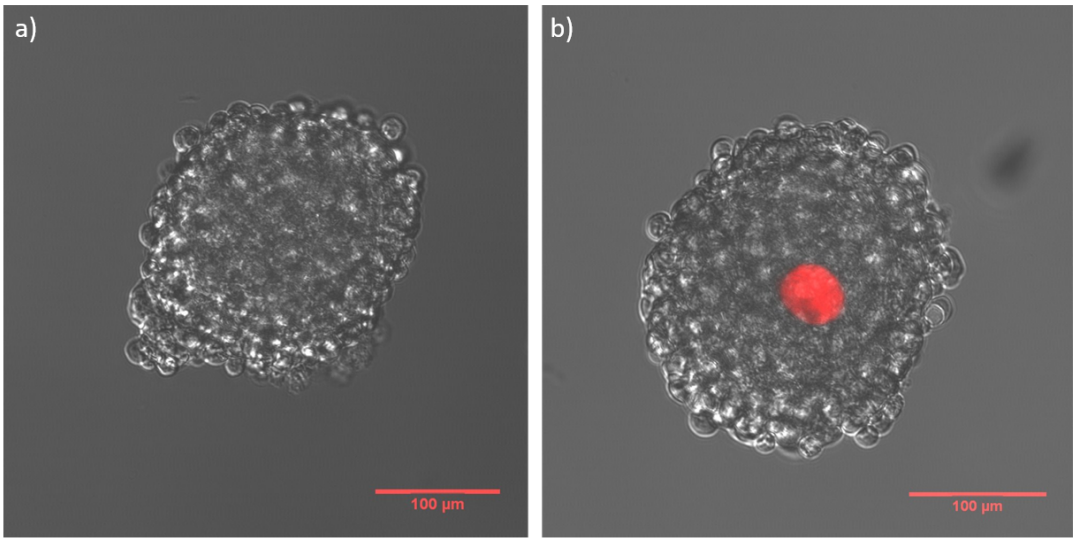

Figure 4.3: a) A 4T1 MCTS cultured using the hanging droplet technque b) A 4T1 spheroid injected with magnetic droplets.

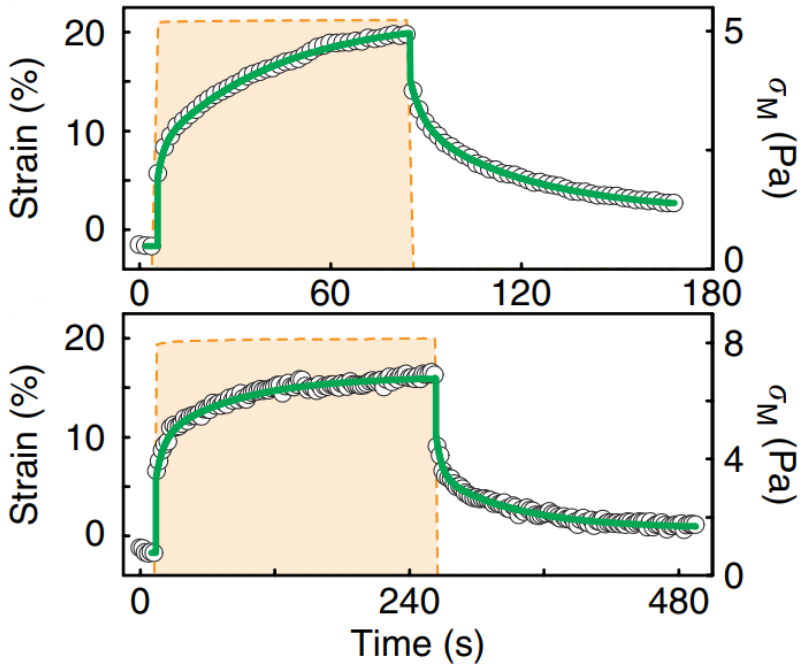

Figure 4.4: Stress and Strain data measured from previous experiments done on zebrafish yolk from the Campàs lab, [68]

netic droplets mentioned in section 4.4.1 inside the fluorescently tagged MCTS. Again, time-series experiments are conducted while actuating and relaxing the magnetic droplet

and the contours of the deforming droplet are acquired using an image-processing software programmed using both LabVIEW and the image acquisition software (Zen) after specifying appropriate imaging parameters. The aspect ratios for every time point are calculated for the droplet. The change in the aspect ratio of the magnetic droplet after an actuation can be used to infer the deformation of the surrounding tissues and to infer stress-strain curves. The deformation calculated this way can be used to calculate the storage and loss moduli. A parameter estimation algorithm is implemented to calculate the stiffness and viscosity of the tumor spheroids by fitting the stress and strain to linear visco-elastic models such as the Kelvin-Voigt model, Maxwell model, and the Generalized Maxwell model. Thus changes in the viscosity of the tumor aggregate can be calculated while it is invading.

4.4 Cell Lines Used

A variety of cancer cell lines were investigated for growing the 3D cultures. The following cell lines were considered based on their ability to form good spheroids using the hanging droplet technique based on experiments seen in the literature [70], [71], [72]. A complete list includes;

4.5 Culturing Flourescent Tagged MCTS

All the cell lines specified in Table 4.1 were used to make multi-cellular spheroids. However, only 3 out of the 6 cell lines namely - the HepG2, MCF10ca1a, and the 4T1 cells produce compact spherical spheroids. The MCF7 and MDA MB-231 adhere together so weakly that they do not form acceptable spheroids. The Prostate cancer line PCC3 does form good aggregates but, they are usually oblong (not spherical) and invades in a

Cell Line	Description
MCF 7	ER (Estrogen Receptor) positive Human Breast Cancer Cell Line
MCF10 ca1a	Human Breast Cancer Cell Line
MBA MD-231	Triple Negative Human Breast Cancer Cell Line
PCC3	Human Prostate Cancer Cell Line
HepG2	Human Liver Cancer Cell Line
4T1	Mouse Mammary Cell Line

Table 4.1: List of Cell Lines Considered for Three Dimensional Culture of Tumor Spheroids

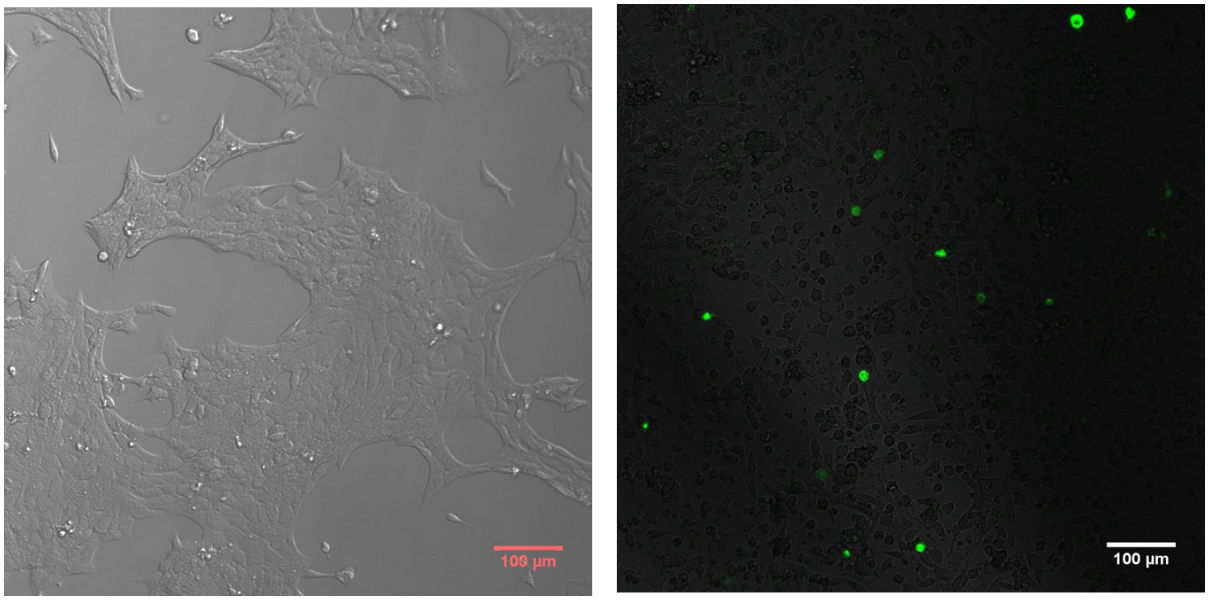

Figure 4.5: Left - a monolayer culture of 4T1 cell line, Right - 4T1 cell lines at the initial stage of transfection.

single-cell manner. As the experiments intended to examine stream-lined finger-like an invasion from an initially spherical aggregate, this cell line was rejected. Hence, the 3 cell lines used for the experiments are the MCF10ca1a, HepG2 and 4T-1 cell lines which were observed to form good spheroids and invade in a finger-like manner. Please see Appendix A for the procedures used to maintain these cell lines. These fluorescently labeled cells

(different colors for nucleus and cell membrane) are used to culture Multi-Cultural Tumor Spheroids (MCTS) via the hanging droplet technique in Petri-dishes (Appendix A.6.1).

Chapter 5

Conclusions and Future Work

The work presented in this Thesis introduces two coarse-grained continuum mechanical models that offer a view into how variations of the internal mechanical properties of the spheroid and how active surface stresses could facilitate tumor invasion and growth. They both use a two-phase moving mesh model of incompressible fluid domains that represent both the spheroid and the micro-environment. They both have proliferation and viscosity profiles dependent on the distance from the spheroid contour - clearly demarcating a necrotic core region and a proliferating rim region. Several interesting physical phenomena were predicted by the model, some of which are observed in experiments.

The overarching hypothesis in the first model is that a solid-to-fluid phase transition facilitates the formation of surface instabilities. This model showed the onset of small buckling instabilities in the lower Capillary number regimes ($Ca = 0.01$), but these were not representative of an invasive phenotype and the most prominent of them did not take place in the paramter regimes expected of a tumor with a necrotic core. To observe this more clearly, these models were simulated using a full 2D model to remove the effect of the axial symmetry boundary condition imposed by COMSOL in the first model.

Here, the wavelength of the buckling instabilities observed earlier was found to depend on the parameter $\frac{\lambda}{l}$, the ratio of the proliferative rim thickness to the intrinsic length scale of. The properties of these instabilities like the wavelength, curvature variations and the time-scales are dependent on the length of the proliferation rim. The variations in curvature increases as the length of the proliferation decreases. They are reminiscent of creasing instabilities observed in organs that undergo significant invagination, like the human brain. However, it is likely that, the active forces applied by the aggregate greatly contribute to tumor invasion and need to be included.

There are multiple hallmarks of cancer that aids it in its invasion to a different site. This includes the ability of the tumor to fluidize its surrounding matrix and apply active forces using membrane junction proteins on surfaces that can sustain these forces. In both models in this study, the surrounding medium was assumed to be much more fluidized than the tumor aggregate itself (represented by a much lower viscosity). The addition in the second model is the ability of the tumor to apply active stresses normal to its surface and dependent on the local mean curvature as observed experimentally [66]. This introduced instability in the system that showed the tendency of the spheroid to pinch off and leave the primary site. As the geometry becomes highly nonlinear, the moving mesh is unable to accommodate severe topological changes. Consequently, these could not be simulated to large durations of time.

5.1 Future Work

Several different parameter regimes remain to be explored in this model. For instance, the involvement of the tumor micro-environment has been largely ignored. This greatly

limits the scope of this study because it is well documented that tumor aggregates interact actively with their micro-environment by chemical and mechanical signaling. Some parameters to consider first would be the viscosity of the micro-environment and examine how profiles in them could contribute to tumor invasion. An interesting hypothesis is to coarse-grain the tumor‘s ability to re-model the Extra-Cellular Matrix (ECM) fibers as tracks of low-viscosity regions and perform the same analysis on the instabilities due to proliferation and that induced by active stress. Such a study could complete the circle by investigating both the internal mechanics, surface properties and the tumor micro-environment providing a holistic view of tumor invasion.

Another modification to attempt would be to limit the value of active stresses the cells can experience. This can be done by defining an upper limit to the force function. Currently, active stress is allowed to increase in an unbounded fashion quadratically. This is realistic because there is a physical limit to the amount of force that an invading from of the tumor aggregate can apply on the ECM. Also, varying powers of how the active stress depends on curvature can also be explored. In this case, only the square term was considered while, cubic and fourth powers could show other interesting effects.

Finally, it is interesting to investigate the effects of combining the instabilities induced by proliferation and that by tumor invasion. It is possible that one could be accentuating the other or they could be working against each other. It is also possible that the resulting wavelength could contain frequency components of both types of these instabilities.

This thesis demonstrates how commercial solvers like COMSOL, which is only starting to be explored for solving models for morphogenesis and organogenesis can be used to obtain solutions for complex systems like tumors when the correct mechanical profiles

are incorporated. The present study only implements only a fraction of what COMSOL is truly capable of. There are diverse mathematical interfaces that could be computationally more expensive but will be capable of handling the large non-linearities observed in the previous results.

As mentioned earlier, the moving mesh module is incapable of solving the model when there are significant topological variations. Two types of multi-phase models that could simulate this are the level-set technique and the phase-field techniques. These can model deformations that could lead to the separation of one domain into two and should be explored. The reason why this was not used in the present study was primarily that, it was computationally expensive and they were diffuse-interface techniques.

A different set of tools that COMSOL offers are those for Fluid-Structure Interactions. In many previous studies, scientists have modeled the tumor aggregate and the spheroid as solid domains with widely varying material properties. COMSOL offers different material property models which vary from linear elastic, visco-elastic, hyperelastic models, etc. These might offer interesting results by expanding the mechanical parameters considered. For instance, rheological models can include storage moduli and loss moduli and parametric sweeps could be executed to observe instabilities due to varying them. The property of elasticity has been largely ignored in the present study. The multiphysics modules for biot poroelasticity and subsurface flow could also be potentially used to model tumor invasion.

Finally, COMSOL's versatility in specifying variational constraints and equations using their weak contributions node can be of great use. Some of the interesting work done using them pertinent to this study would that of were an Oldroyd B fluid was simulated.

Although it required multiple stabilization techniques, it is a nice model instructive of how to start modeling complex fluids in COMSOL. It would be interesting to model tumor spheroids as Oldroyd-B fluids and examine the effect of varying the Wissenberg number.

In Conclusion, the work presented here explores both the internal mechanics of a simplified tumor model in two different types of geometry and also the evolution of the tumor aggregate contours and the parameters that control them. Hence, it provides insight into both the dynamics of the tumor bulk and its surface properties. Multiple avenues remain to be explored in both the existing model and by using modeling techniques that are based on radically different mathematical frameworks, which in the future will surely elicit interesting and exciting results.

Appendix A

Cell Culture Methods

A.1 Unfreezing Cells

The cell lines which were stored as cryovials were thawed in a hot water bath or an armor bead bath just until the frozen cell-freezing medium became liquid. The thawed vial is wiped with alcohol and transferred into the Biosafety cabinet. The thawed cell culture and freezing medium mixture was resuspended in 10 mL of the corresponding culture medium (DMEM for all cell lines mentioned in Table 4.1 except for 4T1 which uses RPMI culture medium). The resuspended cells were then spun down using a centrifuge at 1200 rpm for 5 minutes into pellet form. The supernatant was removed and the remaining pellet was once again resuspended using $5mL$ of the corresponding culture medium. The suspension was then transferred into a $T-25$ culture flask and incubated at 37 ^{o} C with 5 % Carbon Dioxide. The culture flask is inspected daily and the culture media may be changed as required, depending on how fast the cell line grows and consumes nutrients.

A.2 Passaging of Confluent Cell Lines

The previous subsection provides details about the unfreezing of cryo-preserved cells. After the growth of the cell line stabilizes, the cells need to be passaged periodically when they achieve confluency. This is necessary to maintain the overall health of the cell line. Confluency is measured in the percentage area of the flask in which the cell lines are attached. The rule-of-thumb level of confluency for passaging cell lines is 70-80 %.

The exact cell division times vary for different cell lines. For instance, the MCF 7 line divides once every 36 hours while the PC3 line divides in 24 hours. Depending on the cell division times and assuming that the correct incubation conditions and culture media were provided without any contamination, the $T-25$ culture flasks would achieve 70-80 % confluence in nearly 3 days. The culture flasks are inspected every day to check the level of confluency and they are passaged if they reach $70-80\%$ confluency.

The aseptic technique is followed when bringing items into the Biosafety Cabinet - all items are wiped with alcohol and Kimwipes before using them. After cleaning the confluent flasks, the older culture media is removed from them using Pasteur pipets. The pipet transfers the media into a waste disposal system. This does not disturb the cells as they are attached to the bottom of the culture flasks. The attached cells are then rinsed with Phosphate-Buffered Saline (PBS) solution $(3-5mL)$ to remove any remnants of the media or any other impurities. The PBS is removed using a Pasteur pipet and the *cell dissociation buffer* or *trypsin* $(3-5mL)$ is added to detach the cells from the bottom of the culture flask. The buffer contains chemicals that cleave the bonds between adjacent cells and between the cell and the flask. The flask containing the dissociation buffer is incubated at 37^o C with 5% Carbon dioxide for 10 minutes. For most cell lines, this

detaches the cells and can be seen floating inside the culture flask under a microscope. If the cell line is highly adherent, gently tapping it by hand should remove them. The detached cells are rinsed with either PBS (for cell dissociation buffer) or culture media (if trypsinized) and transferred to a 15 mL falcon tube (conical centrifuge tube). The falcon tube is centrifuged at 1200 rpm for 5 minutes to form a pellet of the cells. The falcon tube is wiped with alcohol and brought into the cell culture hood and the supernatant is removed using a Pasteur pipet. The pellet is resuspended using $3 - 5mL$ of media.

The cells are now counted using a cell hemacytometer. The cell suspension obtained from step is agitated to ensure uniform distribution of cells and 90 μL of the cell suspension is aspirated with a micropipette and transferred to a microfuge tube. $10\mu L$ of Trypan-Blue solution is added to the cells and the mixture is shaken. From the microfuge tube, 10 μL of stained cells are aspirated and transferred to between the cell hemacytometer and the cover glass. The hemacytometer is inverted and the cells are counted in either the central grid or the sum of the number of cells in the four top and bottom corners and then averaged. This number multiplied by 10000 gives the density of cells inside the cell suspension falcon tube.

Using the calculated cell density, the required number of cells are transferred to a new T-25 flask. Barring unusual conditions such as very low cells counts, 500000 cells were transferred during each passage into the new flasks. This was done by calculating the required volume of the cells to maintain this count. T-25 flasks are seeded with a total volume 5 mL including both cells and culture media. If there is any remaining volume after the transfer of cells, cell culture media is added to raise it to $5mL$. The flasks were labeled with the cell line name, the passage number and the date of passaging along with any additional information required.

A.3 Cryopreservation of Cell Lines

Cryopreservation is intended for long-term storage of cell lines. The cell lines were cultured in larger T-75 culture flasks. The cells are resuspended in a similar procedure as in a passage which includes detachment, pelleting and subsequent resuspension. The cells are counted and the corresponding volume for 1 million cells is calculated. The cells are centrifuged again and resuspended in cell-freezing buffer of the same volume used for resuspension in the previous step. The volume calculated, for 1 million cells calculated before, is transferred to cryovials and the remaining volume is filled with culture media to raise the total volume to 1 mL. The cryovials are then stored in a -80^{o}C refrigerator.

A.4 Transfection of Cell Lines to Improve Imaging

The spheroids cultured from the afore-mentioned cell lines will be injected with non-magnetic or magnetic droplets. To measure the strain experienced by these droplets and consequently, the surrounding tissues, the cell lines are transfected with GFP, mCherry, and mPlum, along with a kanamycin antibiotic-resistant gene. This is done so that cells not expressing these transfections are selected out and a colony of cells expressing these fluorescent proteins can be obtained. The nucleus and the cell membrane are tagged with different fluorescent proteins - GFP for the nucleus and either mCherry or mPlum for the cell membrane.

A.5 3D Cell Culture of Tumor Spheroids

Multi-cellular Spheroids (MCS) are in-vitro models of cancer aggregates inside a living system. They are composed of cells held together by inter-cellular forces and can be cultured using a variety of techniques. The technique adopted in the present study is called the hanging droplet technique and will be described shortly. The section also describes the advantage of using Multi-Cellular Spheroids over conventional monolayer cultures and describes some of the basic physiological properties of these aggregates.

A.6 Culturing 3 Dimensional Multi-cellular Spheroids

There are a variety of techniques available to culture 3 Dimensional Tumor Spheroids. Some of them include the use of bio-reactors [73], [74], the use of microfluidic channels [75], [76], using biopolymer matrices such as agarose or matrigel to compact colonies of dividing cells to form spherical aggregates [77], [78]. However, in this study, a technique called the hanging droplet technique is used to generate tumor spheroids [72]. This method is chosen because of its simplicity and its ability to form a large number of spheroids using a small number of reagents. Its procedure is described as follows;

A.6.1 The Hanging Droplet Technique

After passaging cells at 70-80% confluence, the cell suspension containing cells and media is retained. Using the cell density calculated during the passaging step, the volume of cell suspension for each hanging drop is calculated based on the number of cells per spheroid. The number of cells per spheroid is decided by the desired radius of each spheroid. The radius increases with the number of cells. For a spheroid of $200\mu m$ radius,

1500 cells need to be seeded in each hanging droplet. The volume of cell suspension for each droplet is calculated and raised to a total volume of $15\mu L$. The volume of each component - both cell suspension and the media is multiplied by the required number of spheroids and mixed in a microfuge tube. The mixture is resuspended using a micro-pipet and $15\mu L$ of the mixture is aspirated using the micro-pipet and dispensed onto the inverted cover of a petri dish. Approximately 30 droplets are made in quick succession. Upon making the droplets, the cover is inverted quickly so that cells do not settle on the petri dish and stick to it. The best results are observed when the droplets are made close to the center of the petri-dish cover. The cover is then closed over a pool of culture media (DMEM or RPMI depending on the kind of cells used). This is required to help the cells grow and to let the spheroid form. The shape of the hanging droplet forces the cells to aggregate at the bottom of the drop. This causes the cells to bind together and form tumor spheroids.

Appendix B

Preparation of Sample

B.1 Mixing the components for magnetic oil droplets

The magnetic droplets are composed of a ferrofluid which provides ferrite nanoparticles to help actuate the droplet, Novec 7700 oil as the continuous phase in which a surfactant known as Krytox (PEG-600) is dispersed. The amphiphilic nature of the Krytox (PEG-600) causes it to orient itself with the hydrophobic tail facing into the droplet. This allows the magnetic droplet to maintain its interfacial tension. Further, rhodamine dye is also added to make the droplet visible under confocal microscopy. The components of the magnetic oil are mixed in specific amounts to obtain good actuation and ease of imaging. A metric that is used is the dilution factor. It is calculated based on the amount of ferrofluid.

The dilution factor denotes the number of times by which the stock concentration of ferrofluid should be divided to obtain the concentration of the prepared magnetic oil. Also, the magnetic stress that can be applied by the droplet varies with the square of the dilution factor. The prepared magnetic oil is sealed using a parafilm wrap and stored in

a cool and dark location.

B.2 Inserting the magnetic droplets into the spheroids

B.2.1 Magnetic Oil Droplets

The injection is carried out in an agarose mold patterned with wells to facilitate injection. The agarose is mixed at 2 % by weight and warmed. The warm mixture is then poured out onto a petri dish and the template for the injection mold is inserted into at nearly 45^o C. The template is removed after the agarose fully cross-links and leaves behind a neat array of wells.

When being prepared for injection, the vial containing the magnetic oil is first sonicated for 10 minutes at room temperature. Approximately, $3\mu L$ of the magnetic oil is aspirated and transferred into a pulled-capillary needle. The needle is connected to the conduit of a pico-liter injector. The injection pressure and the injection time of the injector can be changed using the knobs on the device. These two parameters can be manipulated to change the size of the droplets being injected into the spheroid. If there is too much resistance to the ejection of the droplet from the needle, the length of the needle may be reduced. This is done to increase the diameter of the needle to enhance the flow of the magnetic oil. This might also be required to help improve injection because as the diameter of the tip of the needle increases, the bending rigidity of the needle increases and allows easier piercing of the spheroid surface. The injected droplets are controlled to have diameters between $30 - 40\mu m$.

After injection, the agarose wells in the petri-dish containing the injected spheroids

are incubated overnight so that the spheroids can heal. The spheroids are then embedded in collagen the next day for the invasion assay.

B.3 Embedding the Spheroids in a Collagen Matrix

To successfully perform an invasion assay, the aggregate needs to be positioned in the middle of the crosslinked collagen. Several techniques were attempted to accomplish this. One of the methods was to resuspend the spheroid in collagen inside a microfuge tube and to pipet the mixture out onto a mattek dish. The intention was to control the position of the injected spheroid by varying the volume of the collagen used to resuspend the spheroid and by varying the position of the heat sources to cross-link from different directions. However, the spheroid continued to drop through the collagen as the bulk of the collagen remained un-crosslinked in the center despite the surface regions being cross-linked.

Another technique was to sandwich the injected spheroid between two layers of collagen. However, the spheroid seemed to be able to locate the interface between the two differently crosslinked layers of collagen and spread into that interface. This did not enable studying cancer invasion in all directions and the invasion on such a specific plane was thought to bias the experiment and not provide a realistic picture of cancer invasion.

Lately, a technique that has seen success is the use of circular and square glass capillaries. The method is akin to that in light-sheet microscopy where the sample is aspirated with the aid of capillary effects and suspended in the middle of the capillary. Spheroids embedded this way have been observed to invade in a finger-like fashion. However, the curvature of the circular capillary bent the light and obscured the image.

The square capillaries rectify this issue. Having embedded the injected spheroid in the

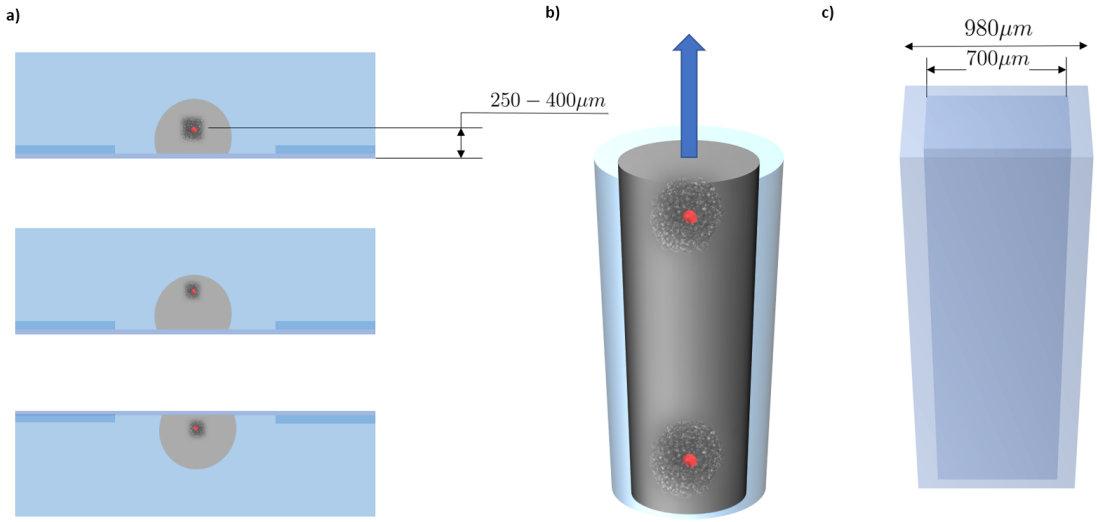

Figure B.1: a) Using Mattek dishes to embed the spheroid. The MCTS is first re-suspended in collagen and is pipetted out onto a Mattek dish. b) The use of circular capillaries to pick up injected MCTS c) Square capillaries that can avoid the bending of light at the center of each face only.

middle of a square glass capillary, relatively better images of the spheroids can be taken. The dimensions of the square capillaries also need to be of a specific dimension such that the spheroid remains within the working distance of the 40X objective which is approximately $400 - 600\mu m$. As square glass capillaries are expensive, alternate materials like PDMS is being investigated to solve this issue. Furthermore, the square glass capillary also has the issue of lack of perfusion of culture media. Without adequate amounts of culture media, the spheroid can vaporize and compromise the whole experiment. To overcome this, 3D printed molds that position the spheroid correctly, with wells that hold media that will diffuse through the collagen matrix to the other side are being explored. Once, the perfusion can be successfully implemented and the actuation and imaging performance improved, the experiments can be conducted to actuate the droplet and simultaneously image them. This enables the calculation of the changes in aspect

ratio to infer tissue deformation and consequently, the viscosity as a function of time.

Bibliography

[1] R. M. Neto-Silva, S. de Beco, and L. A. Johnston, *Evidence for a growth-stabilizing regulatory feedback mechanism between myc and yorkie, the drosophila homolog of yap*, *Developmental cell* **19** (2010), no. 4 507–520.

[2] K. F. Harvey, X. Zhang, and D. M. Thomas, *The hippo pathway and human cancer*, *Nature Reviews Cancer* **13** (2013), no. 4 246.

[3] X. Zhang, J. George, S. Deb, J. Degoutin, E. Takano, S. Fox, D. Bowtell, and K. Harvey, *The hippo pathway transcriptional co-activator, yap, is an ovarian cancer oncogene*, *Oncogene* **30** (2011), no. 25 2810.

[4] D. Hanahan and R. A. Weinberg, *Hallmarks of cancer: the next generation*, *cell* **144** (2011), no. 5 646–674.

[5] Y. A. Fouad and C. Aanei, *Revisiting the hallmarks of cancer*, *American journal of cancer research* **7** (2017), no. 5 1016.

[6] J. J. Sleeboom, H. E. Amirabadi, P. Nair, C. M. Sahlgren, and J. M. Den Toonder, *Metastasis in context: modeling the tumor microenvironment with cancer-on-a-chip approaches*, *Disease models & mechanisms* **11** (2018), no. 3 dmm033100.

[7] S. Kumar and V. M. Weaver, *Mechanics, malignancy, and metastasis: the force journey of a tumor cell*, *Cancer and Metastasis Reviews* **28** (2009), no. 1-2 113–127.

[8] P. Roca-Cusachs, V. Conte, and X. Trepat, *Quantifying forces in cell biology*, *Nature cell biology* **19** (2017), no. 7 742.

[9] A. Mongera, P. Rowghanian, H. J. Gustafson, E. Shelton, D. A. Kealhofer, E. K. Carn, F. Serwane, A. A. Lucio, J. Giammona, and O. Campàs, *A fluid-to-solid jamming transition underlies vertebrate body axis elongation*, *Nature* **561** (2018), no. 7723 401.

[10] S. Dupont, L. Morsut, M. Aragona, E. Enzo, S. Giulitti, M. Cordenonsi, F. Zanconato, J. Le Digabel, M. Forcato, S. Bicciato, *et. al.*, *Role of yap/taz in mechanotransduction*, *Nature* **474** (2011), no. 7350 179.

[11] B. C. Low, C. Q. Pan, G. Shivashankar, A. Bershadsky, M. Sudol, and M. Sheetz, *Yap/taz as mechanosensors and mechanotransducers in regulating organ size and tumor growth*, *FEBS letters* **588** (2014), no. 16 2663–2670.

[12] Z. N. Demou, *Gene expression profiles in 3d tumor analogs indicate compressive strain differentially enhances metastatic potential*, *Annals of biomedical engineering* **38** (2010), no. 11 3509–3520.

[13] A. Carisey, R. Tsang, A. M. Greiner, N. Nijenhuis, N. Heath, A. Nazgiewicz, R. Kemkemer, B. Derby, J. Spatz, and C. Ballestrem, *Vinculin regulates the recruitment and release of core focal adhesion proteins in a force-dependent manner*, *Current biology* **23** (2013), no. 4 271–281.

[14] V. Swaminathan, K. Mythreye, E. T. O'Brien, A. Berchuck, G. C. Blobe, and R. Superfine, *Mechanical stiffness grades metastatic potential in patient tumor cells and in cancer cell lines*, *Cancer research* **71** (2011), no. 15 5075–5080.

[15] M. J. Paszek, N. Zahir, K. R. Johnson, J. N. Lakins, G. I. Rozenberg, A. Gefen, C. A. Reinhart-King, S. S. Margulies, M. Dembo, D. Boettiger, *et. al.*, *Tensional homeostasis and the malignant phenotype*, *Cancer cell* **8** (2005), no. 3 241–254.

[16] G. Helmlinger, P. A. Netti, H. C. Lichtenbeld, R. J. Melder, and R. K. Jain, *Solid stress inhibits the growth of multicellular tumor spheroids*, *Nature biotechnology* **15** (1997), no. 8 778.

[17] D. S. Chorev, O. Moscovitz, B. Geiger, and M. Sharon, *Regulation of focal adhesion formation by a vinculin-arp2/3 hybrid complex*, *Nature communications* **5** (2014) 3758.

[18] W. H. Goldmann, *Role of vinculin in cellular mechanotransduction*, *Cell biology international* **40** (2016), no. 3 241–256.

[19] C. Grashoff, B. D. Hoffman, M. D. Brenner, R. Zhou, M. Parsons, M. T. Yang, M. A. McLean, S. G. Sligar, C. S. Chen, T. Ha, *et. al.*, *Measuring mechanical tension across vinculin reveals regulation of focal adhesion dynamics*, *Nature* **466** (2010), no. 7303 263.

[20] Q. K. Chen, K. Lee, D. C. Radisky, and C. M. Nelson, *Extracellular matrix proteins regulate epithelial–mesenchymal transition in mammary epithelial cells*, *Differentiation* **86** (2013), no. 3 126–132.

[21] F. Kai, H. Laklai, and V. M. Weaver, *Force matters: biomechanical regulation of cell invasion and migration in disease*, *Trends in cell biology* **26** (2016), no. 7 486–497.

[22] K. R. Levental, H. Yu, L. Kass, J. N. Lakins, M. Egeblad, J. T. Erler, S. F. Fong, K. Csiszar, A. Giaccia, W. Weninger, *et. al.*, *Matrix crosslinking forces tumor progression by enhancing integrin signaling*, *Cell* **139** (2009), no. 5 891–906.

[23] C. Voutouri, F. Mpekris, P. Papageorgis, A. D. Odysseos, and T. Stylianopoulos, *Role of constitutive behavior and tumor-host mechanical interactions in the state of stress and growth of solid tumors*, *PloS one* **9** (2014), no. 8 e104717.

[24] Y. Li, M. J. Fanous, K. A. Kilian, and G. Popescu, *Quantitative phase imaging reveals matrix stiffness-dependent growth and migration of cancer cells*, *Scientific reports* **9** (2019), no. 1 248.

[25] A. Kostic, C. D. Lynch, and M. P. Sheetz, *Differential matrix rigidity response in breast cancer cell lines correlates with the tissue tropism*, *PloS one* **4** (2009), no. 7 e6361.

[26] N. S. Waleh, J. Gallo, T. D. Grant, B. J. Murphy, R. H. Kramer, and R. M. Sutherland, *Selective down-regulation of integrin receptors in spheroids of squamous cell carcinoma*, *Cancer research* **54** (1994), no. 3 838–843.

[27] R.-Z. Lin, L.-F. Chou, C.-C. M. Chien, and H.-Y. Chang, *Dynamic analysis of hepatoma spheroid formation: roles of e-cadherin and β1-integrin*, *Cell and tissue research* **324** (2006), no. 3 411–422.

[28] M. T. Santini, G. Rainaldi, and P. L. Indovina, *Apoptosis, cell adhesion and the extracellular matrix in the three-dimensional growth of multicellular tumor spheroids*, *Critical reviews in oncology/hematology* **36** (2000), no. 2-3 75–87.

[29] M. Nakamura, T. Shinji, K. Ujike, S. Hirasaki, N. Koide, and T. Tsuji, *Cytoskeletal inhibitors, anti-adhesion molecule antibodies, and lectins inhibit hepatocyte spheroid formation*, *Acta medica Okayama* **56** (2002), no. 1 43–50.

[30] B. A. Bao, C. P. Lai, C. C. Naus, and J. R. Morgan, *Pannexin1 drives multicellular aggregate compaction via a signaling cascade that remodels the actin cytoskeleton*, *Journal of Biological Chemistry* **287** (2012), no. 11 8407–8416.

[31] A. D. Conger and M. C. Ziskin, *Growth of mammalian multicellular tumor spheroids*, *Cancer Research* **43** (1983), no. 2 556–560.

[32] X. Cui, Y. Hartanto, and H. Zhang, *Advances in multicellular spheroids formation*, *Journal of the Royal Society Interface* **14** (2017), no. 127 20160877.

[33] R. Edmondson, J. J. Broglie, A. F. Adcock, and L. Yang, *Three-dimensional cell culture systems and their applications in drug discovery and cell-based biosensors*, *Assay and drug development technologies* **12** (2014), no. 4 207–218.

[34] R. Durand and R. Sutherland, *Effects of intercellular contact on repair of radiation damage*, *Experimental cell research* **71** (1972), no. 1 75–80.

[35] E. R. Boghaert, X. Lu, P. E. Hessler, T. P. McGonigal, A. Oleksijew, M. J. Mitten, K. Foster-Duke, J. A. Hickson, V. E. Santo, C. Brito, *et. al.*, *The volume of three-dimensional cultures of cancer cells invitro influences transcriptional profile differences and similarities with monolayer cultures and xenografted tumors*, *Neoplasia* **19** (2017), no. 9 695–706.

[36] D. R. Grimes, P. Kannan, A. McIntyre, A. Kavanagh, A. Siddiky, S. Wigfield, A. Harris, and M. Partridge, *The role of oxygen in avascular tumor growth*, *PloS one* **11** (2016), no. 4 e0153692.

[37] F. Hirschhaeuser, H. Menne, C. Dittfeld, J. West, W. Mueller-Klieser, and L. A. Kunz-Schughart, *Multicellular tumor spheroids: an underestimated tool is catching up again*, *Journal of biotechnology* **148** (2010), no. 1 3–15.

[38] S. L. Ham, P. S. Thakuri, M. Plaster, J. Li, K. E. Luker, G. D. Luker, and H. Tavana, *Three-dimensional tumor model mimics stromal–breast cancer cells signaling*, *Oncotarget* **9** (2018), no. 1 249.

[39] M. Li and J. C. Izpisua Belmonte, *Organoids—preclinical models of human disease*, *New England Journal of Medicine* **380** (2019), no. 6 569–579.

[40] B. H. Lee, M. H. Kim, J. H. Lee, D. Seliktar, N.-J. Cho, and L. P. Tan, *Modulation of huh7. 5 spheroid formation and functionality using modified peg-based hydrogels of different stiffness*, *PloS one* **10** (2015), no. 2 e0118123.

[41] V. Cristini and J. Lowengrub, *Multiscale modeling of cancer: an integrated experimental and mathematical modeling approach*. Cambridge University Press, 2010.

[42] H. Greenspan, *Models for the growth of a solid tumor by diffusion*, *Studies in Applied Mathematics* **51** (1972), no. 4 317–340.

[43] L. Glass, *Instability and mitotic patterns in tissue growth*, *Journal of Dynamic Systems, Measurement, and Control* **95** (1973), no. 3 324–327.

[44] J. Casciari, S. Sotirchos, and R. Sutherland, *Mathematical modelling of microenvironment and growth in emt6/ro multicellular tumour spheroids*, *Cell proliferation* **25** (1992), no. 1 1–22.

[45] H. Byrne and M. A. J. Chaplain, *Growth of nonnecrotic tumors in the presence and absence of inhibitors*, *Mathematical biosciences* **130** (1995), no. 2 151–181.

[46] A. R. Anderson, *A hybrid mathematical model of solid tumour invasion: the importance of cell adhesion*, *Mathematical medicine and biology: a journal of the IMA* **22** (2005), no. 2 163–186.

[47] V. Cristini, H. B. Frieboes, R. Gatenby, S. Caserta, M. Ferrari, and J. Sinek, *Morphologic instability and cancer invasion*, *Clinical Cancer Research* **11** (2005), no. 19 6772–6779.

[48] H. B. Frieboes, X. Zheng, C.-H. Sun, B. Tromberg, R. Gatenby, and V. Cristini, *An integrated computational/experimental model of tumor invasion*, *Cancer research* **66** (2006), no. 3 1597–1604.

[49] S. J. Franks, *Mathematical modelling of tumour growth and stability.* PhD thesis, Nottingham Trent University, 2001.

[50] S. Franks, H. Byrne, J. King, J. Underwood, and C. Lewis, *Modelling the early growth of ductal carcinoma in situ of the breast*, *Journal of mathematical biology* **47** (2003), no. 5 424–452.

[51] A. Friedman, *Free boundary problems associated with multiscale tumor models*, *Mathematical Modelling of Natural Phenomena* **4** (2009), no. 3 134–155.

[52] D. Ambrosi and F. Mollica, *On the mechanics of a growing tumor*, *International journal of engineering science* **40** (2002), no. 12 1297–1316.

[53] C. Breward, H. Byrne, and C. Lewis, *The role of cell-cell interactions in a two-phase model for avascular tumour growth*, *Journal of Mathematical Biology* **45** (2002), no. 2 125–152.

[54] T. Roose, P. A. Netti, L. L. Munn, Y. Boucher, and R. K. Jain, *Solid stress generated by spheroid growth estimated using a linear poroelasticity model*, *Microvascular research* **66** (2003), no. 3 204–212.

[55] M. Chaplain and B. Sleeman, *Modelling the growth of solid tumours and incorporating a method for their classification using nonlinear elasticity theory*, *Journal of mathematical biology* **31** (1993), no. 5 431–473.

[56] C. Chen, H. Byrne, and J. King, *The influence of growth-induced stress from the surrounding medium on the development of multicell spheroids*, *Journal of mathematical biology* **43** (2001), no. 3 191–220.

[57] D. A. Hormuth, J. A. Weis, S. L. Barnes, M. I. Miga, E. C. Rericha, V. Quaranta, and T. E. Yankeelov, *A mechanically coupled reaction–diffusion model that incorporates intra-tumoural heterogeneity to predict in vivo glioma growth*, *Journal of The Royal Society Interface* **14** (2017), no. 128 20161010.

[58] P. Macklin, S. McDougall, A. R. Anderson, M. A. Chaplain, V. Cristini, and J. Lowengrub, *Multiscale modelling and nonlinear simulation of vascular tumour growth*, *Journal of mathematical biology* **58** (2009), no. 4-5 765–798.

[59] V. Cristini, X. Li, J. S. Lowengrub, and S. M. Wise, *Nonlinear simulations of solid tumor growth using a mixture model: invasion and branching*, *Journal of mathematical biology* **58** (2009), no. 4-5 723.

[60] E. Khain and L. M. Sander, *Dynamics and pattern formation in invasive tumor growth*, *Physical review letters* **96** (2006), no. 18 188103.

[61] L. Preziosi and A. Tosin, *Multiphase and multiscale trends in cancer modelling*, *Mathematical Modelling of Natural Phenomena* **4** (2009), no. 3 1–11.

[62] P. Tracqui, *Biophysical models of tumour growth*, *Reports on Progress in Physics* **72** (2009), no. 5 056701.

[63] L. B. Edelman, J. A. Eddy, and N. D. Price, *In silico models of cancer*, *Wiley Interdisciplinary Reviews: Systems Biology and Medicine* **2** (2010), no. 4 438–459.

[64] T. Roose, S. J. Chapman, and P. K. Maini, *Mathematical models of avascular tumor growth*, *SIAM review* **49** (2007), no. 2 179–208.

[65] C. M. Nelson, J. P. Gleghorn, M.-F. Pang, J. M. Jaslove, K. Goodwin, V. D. Varner, E. Miller, D. C. Radisky, and H. A. Stone, *Microfluidic chest cavities reveal that transmural pressure controls the rate of lung development*, *Development* **144** (2017), no. 23 4328–4335.

[66] N. Gjorevski, A. S. Piotrowski, V. D. Varner, and C. M. Nelson, *Dynamic tensile forces drive collective cell migration through three-dimensional extracellular matrices*, *Scientific reports* **5** (2015) 11458.

[67] O. Campàs, T. Mammoto, S. Hasso, R. A. Sperling, D. O'connell, A. G. Bischof, R. Maas, D. A. Weitz, L. Mahadevan, and D. E. Ingber, *Quantifying cell-generated mechanical forces within living embryonic tissues*, *Nature methods* **11** (2014), no. 2 183.

[68] F. Serwane, A. Mongera, P. Rowghanian, D. A. Kealhofer, A. A. Lucio, Z. M. Hockenbery, and O. Campàs, *In vivo quantification of spatially varying mechanical properties in developing tissues*, *Nature methods* **14** (2017), no. 2 181.

[69] A. A. Lucio, A. Mongera, E. Shelton, R. Chen, A. M. Doyle, and O. Campàs, *Spatiotemporal variation of endogenous cell-generated stresses within 3d multicellular spheroids*, *Scientific reports* **7** (2017), no. 1 12022.

[70] G. Y. Lee, P. A. Kenny, E. H. Lee, and M. J. Bissell, *Three-dimensional culture models of normal and malignant breast epithelial cells*, *Nature methods* **4** (2007), no. 4 359.

[71] E. B. Berens, J. M. Holy, A. T. Riegel, and A. Wellstein, *A cancer cell spheroid assay to assess invasion in a 3d setting*, *JoVE (Journal of Visualized Experiments)* (2015), no. 105 e53409.

[72] J. M. Kelm, N. E. Timmins, C. J. Brown, M. Fussenegger, and L. K. Nielsen, *Method for generation of homogeneous multicellular tumor spheroids applicable to a wide variety of cell types*, *Biotechnology and bioengineering* **83** (2003), no. 2 173–180.

[73] H. W. Rhee, H. E. Zhau, S. Pathak, A. S. Multani, S. Pennanen, T. Visakorpi, and L. W. Chung, *Permanent phenotypic and genotypic changes of prostate cancer cells cultured in a three-dimensional rotating-wall vessel*, *In Vitro Cellular & Developmental Biology-Animal* **37** (2001), no. 3 127–140.

[74] G. A. Thouas, M. C. Thompson, K. G. Contreras, K. Y. Liow, K. B. Tan, and K. Hourigan, *Improved oxygen diffusion and mechanical aggregation of tumor colonies in a novel stirred mini-bioreactor*, in *2008 30th Annual International Conference of the IEEE Engineering in Medicine and Biology Society*, pp. 3586–3589, IEEE, 2008.

[75] L. Yu, M. C. Chen, and K. C. Cheung, *Droplet-based microfluidic system for multicellular tumor spheroid formation and anticancer drug testing*, *Lab on a Chip* **10** (2010), no. 18 2424–2432.

[76] A. Y. Hsiao, Y.-s. Torisawa, Y.-C. Tung, S. Sud, R. S. Taichman, K. J. Pienta, and S. Takayama, *Microfluidic system for formation of pc-3 prostate cancer co-culture spheroids*, *Biomaterials* **30** (2009), no. 16 3020–3027.

[77] C. Fischbach, R. Chen, T. Matsumoto, T. Schmelzle, J. S. Brugge, P. J. Polverini, and D. J. Mooney, *Engineering tumors with 3d scaffolds*, *Nature methods* **4** (2007), no. 10 855.

[78] C. S. Szot, C. F. Buchanan, J. W. Freeman, and M. N. Rylander, *3d in vitro bioengineered tumors based on collagen i hydrogels*, *Biomaterials* **32** (2011), no. 31 7905–7912.